Formation and pathways of dense water in the Nordic Seas based on a regional inversion

Ailin Brakstad [a,b,*], Geoffrey Gebbie [c], Kjetil Våge [a,b], Emil Jeansson [d,b], Sólveig Rósa Ólafsdóttir [e]

[a] *Geophysical Institute, University of Bergen, Norway*
[b] *Bjerknes Centre for Climate Research, Bergen, Norway*
[c] *Woods Hole Oceanographic Institution, Woods Hole, USA*
[d] *NORCE Norwegian Research Centre, Bergen, Norway*
[e] *Marine and Freshwater Research Institute, Reykjavik, Iceland*

ARTICLE INFO

ABSTRACT

Dense waters formed in the Nordic Seas spill across gaps in the Greenland-Scotland Ridge into the abyss of the North Atlantic to feed the lower limb of the Atlantic Meridional Overturning Circulation. The overflow water transport is well known, but open questions remain regarding where and how the dense overflow waters are formed and transported to the ridge. Here we develop a regional high-resolution version of an inverse method called Total Matrix Intercomparison, which combines hydrographic and geochemical tracer observations between 2000 and 2019 to resolve the pathways that connect the overflows to their origins. Consistent with previous studies we find two main pathways feeding the Denmark Strait Overflow Water (DSOW): the East Greenland Current and the North Icelandic Jet. Most of the water supplied by the North Icelandic Jet originates in the Greenland Sea (82 ± 2%) and flows southward along an outer core of the East Greenland Current, as well as along a previously unknown pathway crossing the Jan Mayen Ridge into the Iceland Sea. In total, 39 ± 2% of the DSOW originates in the Greenland Sea, while the Iceland Sea and the Atlantic Domain of the Nordic Seas account for 20 ± 3% and 19 ± 2%, respectively. The majority of the Faroe Bank Channel Overflow Water originates in the Greenland Sea (46 ± 8%) and the Arctic Ocean (25 ± 9%). These dense waters approach the sill in the Iceland-Faroe Slope Jet and along the eastern side of the Jan Mayen Ridge. The inversion reveals unprecedented details on the upstream sources and pathways of the overflows, which have not previously been obtained using observations.

1. Introduction

The overflows from the Nordic Seas are a main source of dense water to the lower limb of the Atlantic Meridional Overturning Circulation (AMOC, Lozier et al., 2019; Chafik and Rossby, 2019; Tsubouchi et al., 2021). Warm and saline Atlantic Water flows northwards into the Nordic Seas (Fig. 1), where intense heat loss in winter transforms the water into colder and denser water masses that return southwards through gaps in the Greenland-Scotland Ridge (GSR) as overflow plumes. The largest overflow plume passes through Denmark Strait between Greenland and Iceland (3.2 Sv, 1 Sv ≡ 10^6 m³ s⁻¹), while most of the overflow east of Iceland (2.0 Sv) flows southwards through the Faroe Bank Channel (Østerhus et al., 2019). The overflow through these two passages combine to approximately 90% of the total overflow water, generally defined as water denser than $\sigma_\Theta = 27.8$ kg m⁻³ (Dickson and Brown, 1994). The sources and upstream pathways of the dense

water masses feeding these two overflows are not as well known as the transports across the ridge, although both are of key importance for better understanding the sensitivity of the AMOC to a warming climate.

Dense waters are formed in the Nordic Seas by several mechanisms. One is the gradual cooling of the Atlantic Water (AW) along the boundary current system around the Nordic Seas and Arctic Ocean (Mauritzen, 1996; Eldevik et al., 2009). Most of the cooling takes place in the Norwegian Sea (Fig. 1, Isachsen et al., 2007), known as the Atlantic Domain of the Nordic Seas because it is characterized by warm and saline AW at the surface (Swift and Aagaard, 1981). The AW branches that flow northwards through the Barents Sea and Fram Strait encircle the Arctic Ocean, and are further cooled and modified during transit (Rudels et al., 1999, 2005). In Fram Strait the branches transporting densified AW, now referred to as Atlantic-origin water (Våge

---
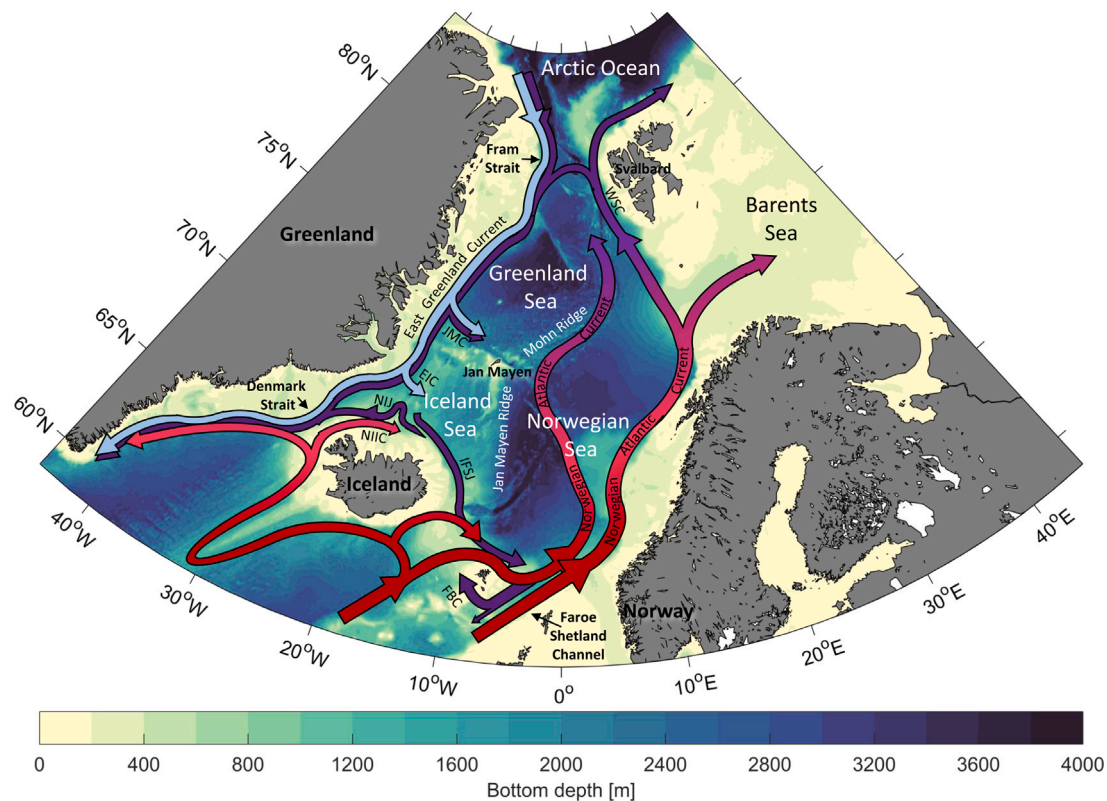
Fig. 1. Schematic circulation in the Nordic Seas. The inflow of warm Atlantic Water is indicated by red arrows, pathways of dense waters are illustrated by dark purple arrows, and southward transport of fresh Polar Surface Water with the East Greenland Current is shown in light blue arrows. The acronyms are: NIIC=North Icelandic Irminger Current; NIJ=North Icelandic Jet; IFSJ=Iceland-Faroe Slope Jet; EIC=East Icelandic Current; JMC=Jan Mayen Current; WSC=West Spitsbergen Current; FBC=Faroe Bank Channel. The background color is the bathymetry from ETOPO1 (Amante and Eakins, 2009).

et al., 2011) merge and return southwards with the East Greenland Current as an intermediate water mass with overflow-water density and a temperature between 0 and 3 °C (Rudels et al., 2005; Håvik et al., 2019). Above the Atlantic-origin water is the cold and fresh Polar Surface Water (PSW), which dominates the entire Greenland shelf along the western Nordic Seas (referred to as the Polar Domain, Swift and Aagaard, 1981). The PSW is too light to contribute directly to the overflows, but gradual mixing with the underlying Atlantic-origin water modifies the upper part of the Denmark Strait overflow plume (e.g., Tanhua et al., 2005; Jeansson et al., 2008; Mastropole et al., 2017).

Another mechanism of dense-water formation is open-ocean convection in the interior Iceland and Greenland Seas (Fig. 1, Swift et al., 1980; Swift and Aagaard, 1981; Marshall and Schott, 1999). These interior seas constitute the Arctic Domain of the Nordic Seas and are separated from the Atlantic and Polar domains by pronounced hydrographic fronts (Helland-Hansen and Nansen, 1909; Swift and Aagaard, 1981). The surface waters in the Arctic Domain are colder and fresher than the AW to the east, but warmer and more saline than the PSW to the west. The region is characterized by weak stratification and substantial heat loss during winter, which results in deep convection and the formation of dense Arctic Intermediate Waters (Swift et al., 1980; Swift and Aagaard, 1981). While these Arctic-origin waters are typically defined as water colder than 0 °C (e.g., Rudels et al., 2005; Jeansson et al., 2008; Våge et al., 2011; Mastropole et al., 2017), intermediate water masses warmer than 0 °C currently form in the central Iceland Sea (Våge et al., 2022).

The densest Arctic-origin water is formed in the Greenland Sea, where wintertime convection at present reaches depths of approximately 500–1500 m (Latarius and Quadfasel, 2010; Lauvset et al., 2018; Brakstad et al., 2019). However, both the depth of convection and the resulting water-mass product have changed substantially over the last 50 years (e.g., Schlosser et al., 1991; Meincke et al., 1992;

Karstensen et al., 2005; Brakstad et al., 2019). Prior to the late 1970s convection occasionally extended to the bottom and produced very cold and dense Greenland Sea Deep Water (GSDW), which was considered the main source of deep water to the entire Nordic Seas (along with deep water from the Arctic Ocean, Helland-Hansen and Nansen, 1909; Malmberg, 1983; Aagaard et al., 1985; Schlosser et al., 1991). There is no evidence of significant renewal of GSDW after 1980, and the main product of convection since the mid-1990s has been the lighter Greenland Sea Arctic Intermediate Water (Karstensen et al., 2005; Ronski and Budéus, 2005; Latarius and Quadfasel, 2010; Brakstad et al., 2019). As a result, a two-layer structure has developed in the Greenland Sea, with a pronounced stratification maximum preventing renewal of GSDW. The distinction between deep and intermediate water masses is typically defined by the potential density anomaly referred to 500 m depth of $\sigma_{0.5} = 30.444$ kg m^{-3} (e.g., Rudels et al., 2005; Jeansson et al., 2008). In the Greenland Sea the depth of this isopycnal coincides with the stratification maximum, which has been located between 1500 and 2000 m depth since the early 2000s (Brakstad et al., 2019).

Dense intermediate and deep waters colder than 0 °C are also supplied to the Nordic Seas from the Arctic Ocean via the East Greenland Current (Rudels et al., 2005; Jeansson et al., 2008, 2017). These water masses are located below the warmer Atlantic-origin water and are mainly a product of AW that has been substantially modified by wintertime convection in the Barents Sea, dense plumes formed on the Arctic shelves, and dense water originally formed in the Nordic Seas that entered the Arctic Ocean in the West Spitsbergen Current (Aagaard et al., 1985; Rudels et al., 1999; Langehaug and Falck, 2012). The fraction of water originally sourced from the Nordic Seas is not well known, but by the time these Arctic Ocean water masses flow southwards through Fram Strait their geochemical properties are distinct from the water occupying the same density range in the Nordic Seas (Jeansson et al., 2008, 2017). The Arctic Ocean deep waters are also warmer and

Table 1

List of data sources, time periods, and parameters included in our analysis, including references. T = temperature, S = salinity, O = oxygen, N = nitrate, and P = phosphate.

Data source	Year(s)	Parameters	Reference
Unified Database for Arctic and Subarctic Hydrography (UDASH)	1980–2015	T and S	Behrendt et al. (2018), https://doi.pangaea.de/10.1594/PANGAEA.872931
International Council for the Exploration of the Seas (ICES)	1950–2019	T, S, O, N, and P	http://ocean.ices.dk/HydChem/HydChem.aspx
Marine Freshwater and Research Institute of Iceland	1950–2018	T, S, O, N, and P	https://sjora.hafro.is
World Ocean Database (WOD)	1966–2018	T, S, O, N, and P	www.noaa.gov/cgi-bin/OS5/SELECT/builder.pl
Global Ocean Data Analysis Project version 2 (GLODAPv2) - 2019	1972–2017	T, S, O, N, and P	Olsen et al. (2016, 2019), https://doi.org/10.25921/xnme-wr20
Argo program	2001–2019	T and S	https://doi.org/10.17882/42182
Norwegian Iceland Seas Experiment database (NISE)	1950–2009	T and S	Nilsen et al. (2008)
Institute of Marine Research (Norwegian Marine Data Centre)	1967–2018	T, S, O, N, and P	https://www.hi.no/en/hi/forskning/research-data-1
Shipboard measurements along the continental slope north of Iceland	2004–2018	T and S	Semper et al. (2019), https://doi.pangaea.de/10.1594/PANGAEA.903535
Iceland-Greenland Seas Project	2018	T, S, O, N, and P	Renfrew et al. (2019)

more saline than the GSDW. After the GSDW formation ceased, the inflow of Arctic Ocean deep waters to the Nordic Seas has thus resulted in a general warming at depth (Meincke and Rudels, 1996; Østerhus and Gammelsrød, 1999; Somavilla et al., 2013).

The deep water in the Nordic Seas is located well below the Denmark Strait sill depth (650 m), while intermediate water masses can contribute more directly to the overflow plume. About 2/3 of the Denmark Strait Overflow Water (DSOW) is supplied by the East Greenland Current (Harden et al., 2016). This current mainly transports overflow water of Atlantic origin (Håvik et al., 2019), but also a substantial portion of dense water from the interior basins (Strass et al., 1993; Rudels et al., 2002; Jeansson et al., 2008). The remaining 1/3 of the DSOW, or perhaps closer to 1/2 according to recent work by Semper et al. (2019), is supplied by the North Icelandic Jet (NIJ) that flows along the slope north of Iceland. The NIJ supplies the densest portion of the DSOW (Våge et al., 2011; Mastropole et al., 2017). While (Våge et al., 2011) hypothesized that the NIJ is part of a local overturning loop in the Iceland Sea, later studies suggest that convection in the interior Iceland Sea may not produce sufficiently dense water (Våge et al., 2015, 2022). Based on several shipboard surveys, Semper et al. (2019) found that the bulk of the NIJ transport is associated with a narrow potential density range centered around $\sigma_\Theta = 28.05$ kg m^{-3} (referred to as the NIJ transport mode). Such dense water is presently not formed in the central Iceland Sea, but it is regularly produced farther north in the Greenland Sea (Brakstad et al., 2019; Huang et al., 2020).

The Faroe Bank Channel Overflow Water (FBCOW) is supplied by intermediate and deep water masses from the Norwegian Sea (Fogelqvist et al., 2003; McKenna et al., 2016). However, most of these water masses are not locally formed. The Norwegian Sea Intermediate Water is composed of Arctic-origin water formed in the Iceland and Greenland Seas, Atlantic-origin water, and intermediate waters from the Arctic Ocean (Eldevik et al., 2009; Jeansson et al., 2017). The Norwegian Sea Deep Water is a mixture of deep water from the Greenland Sea and the Arctic Ocean that enters the Norwegian Basin through deep gaps in the Mohn Ridge north of Jan Mayen (Swift and Koltermann, 1988; Hansen and Østerhus, 2000; Somavilla, 2019; Shao et al., 2019; Wang et al., 2021). Olsson et al. (2005) suggested that intermediate Arctic-origin water from the Greenland Sea also enters the Norwegian Basin north of Jan Mayen, and then follows the eastern side of the Jan Mayen Ridge southwards. This southward-flowing current is supported by other observational and numerical studies (e.g., Voet et al., 2010; Serra et al., 2010; Köhl, 2010; Huang et al., 2020; Hátún et al., 2021),

but questions remain regarding the contribution from the current to the FBCOW. The existence of another current flowing from north of Iceland to the Faroe Islands was recently documented by Semper et al. (2020). This current, named the Iceland-Faroe Slope Jet (IFSJ), may account for approximately half of the FBCOW. The water masses transported by the IFSJ have similar hydrographic properties as the NIJ transport mode, which suggests that they have a common source (Semper et al., 2020). Huang et al. (2020) argued that the primary source region for both the NIJ and the IFSJ is the central Greenland Sea. They also found evidence of several southward pathways along the submarine ridge system surrounding the central Iceland Sea. Where and how the dense water exits the Greenland Sea and to what extent these potential pathways feed the NIJ and IFSJ remain unclear. Chafik et al. (2020) suggested that some overflow water may approach the Faroe-Shetland Channel (upstream of the Faroe Bank Channel, Fig. 1) from the eastern margin along the Norwegian slope, but the upstream sources of this water mass are not known.

The relative contributions of the water masses constituting the Denmark Strait and Faroe Bank Channel overflow plumes are also uncertain. The main reason is that traditional decomposition methods are very sensitive to the number of end-members included in the analysis and their specified properties, which can vary substantially in time and space. Here a regional version of the inverse water-mass decomposition method called Total Matrix Intercomparison (TMI, Gebbie and Huybers, 2010; Gebbie, 2014) was developed to investigate the upstream sources of the Nordic Seas dense water. Our focus is particularly on the origin, pathways, and final composition of the overflow water that passes over the GSR in Denmark Strait and the Faroe Bank Channel. The TMI method is not dependent on a few pre-defined source water masses. Instead, every surface location is considered a potential source of overflow water. By combining hydrographic and geochemical tracer observations between 2000 and 2019, the TMI method geometrically connects the water masses constituting the overflow plumes to their origins, which is a major advantage compared to traditional decomposition methods. With the regional high-resolution inversion we could identify the upstream pathways of the overflows and how water from various source regions contributed and mixed along the pathways.

2. Hydrographic and geochemical observations

2.1. Data sources and quality control

Vertical profiles of temperature (T), salinity (S), oxygen (O), nitrate (N), and phosphate (P) were collected from a range of archives (listed in Table 1) over the period 1950–2019 within the domain 58.5–84°N and
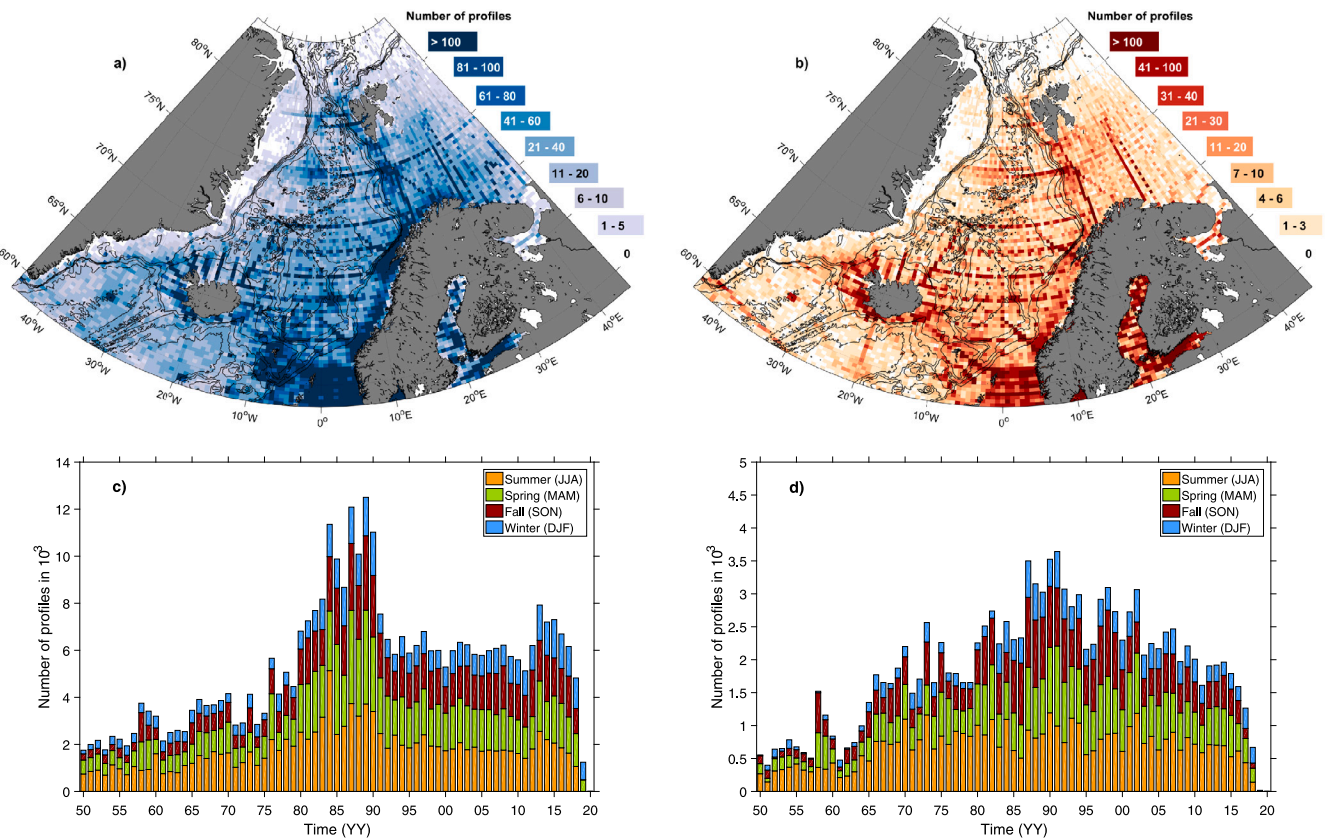
Fig. 2. Distribution of temperature/salinity profiles (a and c) and oxygen/nutrient profiles (b and d). The upper panels show the total number of profiles per 2/3° longitude *x* 1/4° latitude bin since 1950. The bin size is twice the size of the TMI grid cells. The lower panels indicate the number of profiles per year, color coded by season. Note the different color schemes (a and b) and vertical axes (c and d) for the hydrographic and geochemical data distributions.

45°W–45°E. All observations were combined into a single data set and quality controlled. The quality control involves removing duplicates, erroneous profiles, density inversions, and outliers (details are provided in Appendix A). We followed the TEOS-10 standard (IOC et al., 2010) and used Conservative Temperature and Absolute Salinity, hereafter referred to as temperature and salinity, throughout the analysis. The spatial and temporal data distributions of the final quality-controlled data set are shown in Fig. 2. While the spatial variability in water-mass properties is accounted for in the TMI, it is based on the assumption that the observations represent a steady ocean state. Hence, we restricted our analysis to the period 2000–2019. This time period is considered sufficiently stable in terms of dense-water formation and water column structure (i.e. Brakstad et al., 2019; Somavilla, 2019) and is characterized by a generally warmer and more saline water column than the 1980s and 1990s (Skagseth and Mork, 2012; Mork et al., 2014b; Lauvset et al., 2018). The period also contains a sufficient number of observations to adequately constrain the inversion (Fig. 2).

2.2. 2000–2019 climatology of late-winter conditions

To account for seasonal variability in the observations we modified all profiles to represent late-winter (February–April) conditions, when the surface mixed layer is deepest and densest. Late-winter mixed-layer depths determined by Våge et al. (2015) and Brakstad et al. (2019) were used for the Iceland and Greenland Seas, respectively, while a density-difference criterion was employed to estimate the base of the mixed layer for the rest of the domain (Appendix B). The mean 2000–2019 mixed-layer distribution, with a 1/3° longitude *x* 1/8° latitude resolution, is shown in Fig. B.1. The corresponding distributions of late-winter hydrographic and geochemical mixed-layer properties were then used to homogenize each profile from the mean local winter mixed-layer depth to the surface.

The final data set was interpolated onto a three-dimensional grid with a regular horizontal resolution of 1/3° longitude (which ranges from 19 km at 58.5°N to 4 km at 84°N, Fig. 2) and 1/8° latitude (approximately 14 km), and 46 vertical levels with intervals ranging from 10 m near the surface to 250 m at depth (Fig. C.1f). This equals the TMI resolution, which was chosen to resolve the complex bathymetry of the Nordic Seas and the overflow plumes through the deep gaps of the GSR (e.g., Figs. 5 and 13). The resolution is also sufficient to capture the upsloping isopycnals and water-mass properties associated with the narrow NIJ and IFSJ upstream of the sills (Semper et al., 2019, 2020). Since the inversion is observationally constrained and quantifies the net effect of advection and diffusion on the distribution of water masses, it is less prone to errors associated with the resolution compared to numerical simulations that need to parameterize subgrid-scale processes (Gebbie and Huybers, 2010). Details of the gridding procedure are provided in Appendix C. Grid cells without any measurements were kept empty, which implies that they were not used to constrain the inversion. The final gridded product represents the late-winter climatological conditions for the 2000–2019 period. Temporal variability in the observations was accounted for by allowing the TMI inversion to deviate from the climatology within the uncertainty limits of the observations. The uncertainty was estimated based on the number of observations included in each grid cell and their variance, which typically decreases with depth (Appendix C, Fig. C.1). Uncertainties related to the precision of the measurements are small compared to the temporal variability and were not included in our estimates.

3. Total Matrix Intercomparison

3.1. Description of the method

A regional version of the TMI method was developed for the domain 58.5–84°N and 45°W–45°E with the resolution 1/3° longitude, 1/8°

latitude, and 46 vertical levels (Section 2.2, Fig. 2). Apart from the higher resolution, the main difference between this and earlier global versions (Gebbie and Huybers, 2010; Gebbie, 2014) is that it considers both the surface and lateral boundary locations potential sources for the interior water masses in the Nordic Seas. For temperature and salinity we assume that all interior values can be described as some combination of the surface and lateral boundary properties, while oxygen, nitrate, and phosphate are in addition affected by remineralization. The value of any water-mass property c_i at location i in the ocean interior can, in general, be expressed as a linear combination of the properties in the neighboring grid cells plus any local sources or sinks (Gebbie and Huybers, 2010). That is:

$$c_i = \sum_{j=1}^{N} m_{ij} c_j + r q_i, \tag{1}$$

where $N = 6$ is the number of neighboring grid cells, m_{ij} is the fraction of water that originates from cell j with property c_j, and $\sum_{j=1}^{N} m_{ij} = 1$ to assure conservation of mass. Local sources and sinks for oxygen, nitrate, and phosphate are expressed as a product between the interior source term q_i and the stoichiometric ratio r ($\Delta P : 15.5 \Delta N : -170 \Delta O$, Anderson and Sarmiento, 1994; Gebbie and Huybers, 2010).

Following Gebbie and Huybers (2010) and Gebbie (2014), the conservation equation (Eq. (1)) is used to formulate an explicit model for each parameter c as:

$$Ac = d, \tag{2}$$

where c is a vector made from the three-dimensional property field in the Nordic Seas and d is a vector filled with the surface and lateral boundary properties, as well as $r q_i$ for the interior sources and sinks. The matrix A quantifies the strengths of the connections between each location i and its neighbors (the mass fractions m_{ij}). If the pathway matrix A, the boundary properties, and the interior source term q were known, it would be possible to predict the distribution of each parameter c by calculating the inverse of Eq. (2). The goal is to find the solution of A, q, and boundary properties that minimizes the difference between the predicted and observed distributions c. The initial boundary properties and the first guess of A and q are defined in Section 3.2, while Section 3.3 outlines how to solve the inverse problem. The resulting matrix A can be used to diagnose water-mass composition and pathways (Section 3.4), where the pathways represent the steady-state circulation that best fits the observations (i.e., the late-winter hydrographic and geochemical properties in the period 2000–2019). An evaluation of the inversion-to-observational misfits is given in Section 3.5.

3.2. Initial boundary conditions and first guess of pathway matrix A

The initial properties along the surface and lateral boundaries were obtained from the winter-mean gridded climatology described in Section 2.2. Potential modifications to these properties were constrained by the corresponding uncertainty estimated from the observational temporal variability. Measurements of the interior source term q and water-mass pathways A are not available. The interior source term is assumed and enforced to be positive (as a first guess q equals 10^{-3} μmol kg^{-1} everywhere, Gebbie, 2014). The magnitude of q relative to the first guess is also constrained such that larger values only occur if the observations demand it.

The first guess of the pathway matrix A used in previous global TMI inversions (e.g., Gebbie and Huybers, 2010; Gebbie, 2014) represents an isotropic exchange between all grid cells. This means that $m_{ij} = 1/6$ for all grid cells with 6 neighbors. In our regional inversion this first guess resulted in a circulation characterized by excessive diffusivity. Instead we constructed a first guess of A based on the assumption that water tends to flow and mix along geostrophic streamlines and isopycnals (Nøst and Isachsen, 2003). Potential density and geostrophic

velocity fields relative to the surface were derived from the late-winter gridded climatology. Absolute geostrophic velocities were then estimated using annual-mean (2000–2019) surface geostrophic velocity from satellite as reference (gridded altimeter data were obtained from Copernicus Marine Environmental Monitoring Service, http://marine.copernicus.eu). Half of the fraction of water from neighboring grid cells were determined by gradients in density, while the remaining half was determined by gradients in the geostrophic stream function (see Appendix D for details). This first guess substantially improved the solution, in particular the representation of the East Greenland Current.

The sensitivity of the solution to the first guess of A was investigated by altering the weights of the contributions (by ± 10 %) determined by gradients in density versus gradients in the geostrophic stream function. We consider the resulting changes in water-mass composition and pathways, which were relatively minor, an approximate estimate of uncertainty (e.g., Figs. 4, 6, and 14). That is, the error bars of our estimates only represent the uncertainties related to the first guess of A. Uncertainties related to temporal variability in the observations were included as constraints in the inversion to obtain the optimal 2000–2019 winter mean solution.

3.3. Solving the inverse problem

The unknowns that we seek a solution for are the property distributions c (temperature, salinity, oxygen, nitrate, and phosphate), the mass fractions m (which form the pathway matrix A), and the interior source term q. The solution is required to follow the conservation equation (Eq. (1)) for each predicted parameter c and to conserve mass. The solution is then obtained by minimizing the sum of the squared inversion-to-observational misfits, using the method of Lagrange multipliers (Schlitzer, 2007; Gebbie, 2014). The Lagrange multiplier method is specifically designed to handle complex, nonlinear problems such as this, although there is no guarantee that the solution arrives at the overall minimum of the cost function (Köhl and Willebrand, 2002).

The Lagrangian cost function to be minimized is constrained by the conservation equations, the inversion-to-observational misfits weighted by the observational uncertainty, as well as other non-observational constraints on the predicted distributions c, such as a stably stratified water column, temperatures above freezing, and non-negative values for salinity and the geochemical parameters (see supplementary material in Gebbie, 2014, for details). The minimum of the Lagrangian function is found by setting the partial derivatives with respect to c, m, and q equal to zero. This results in a set of adjoint equations that yield information about how the Lagrangian function will change given a change in the pathway matrix A, the initial boundary conditions, and the interior source term q. This information is then used to iteratively improve the Lagrangian function by a quasi-Newton gradient descent method (Nocedal, 1980; Gilbert and Lemaréchal, 1989; Gebbie, 2014).

3.4. Diagnosing water-mass composition and pathways

The optimized pathway matrix A was used to diagnose the composition and upstream pathways of the overflow water at the GSR. Information about the fraction of water (g) sourced from a particular surface or lateral boundary location (b_i) can be obtained by releasing a passive dye at that boundary location. The three-dimensional distribution of dye concentrations equals g and is found directly from the inverse of Eq. (2) ($g = A^{-1}b$, Gebbie and Huybers, 2010), where b equals one at location i and zero elsewhere. The volume of overflow water originating from location i (V) can then be estimated as the sum of the volume in each overflow water grid cell v multiplied by the fraction g:

$$V = v^T g. \tag{3}$$

Our ultimate goal is to determine the amount of overflow water originating from each boundary location, but it would be very inefficient to compute the distribution of g for every single boundary point.
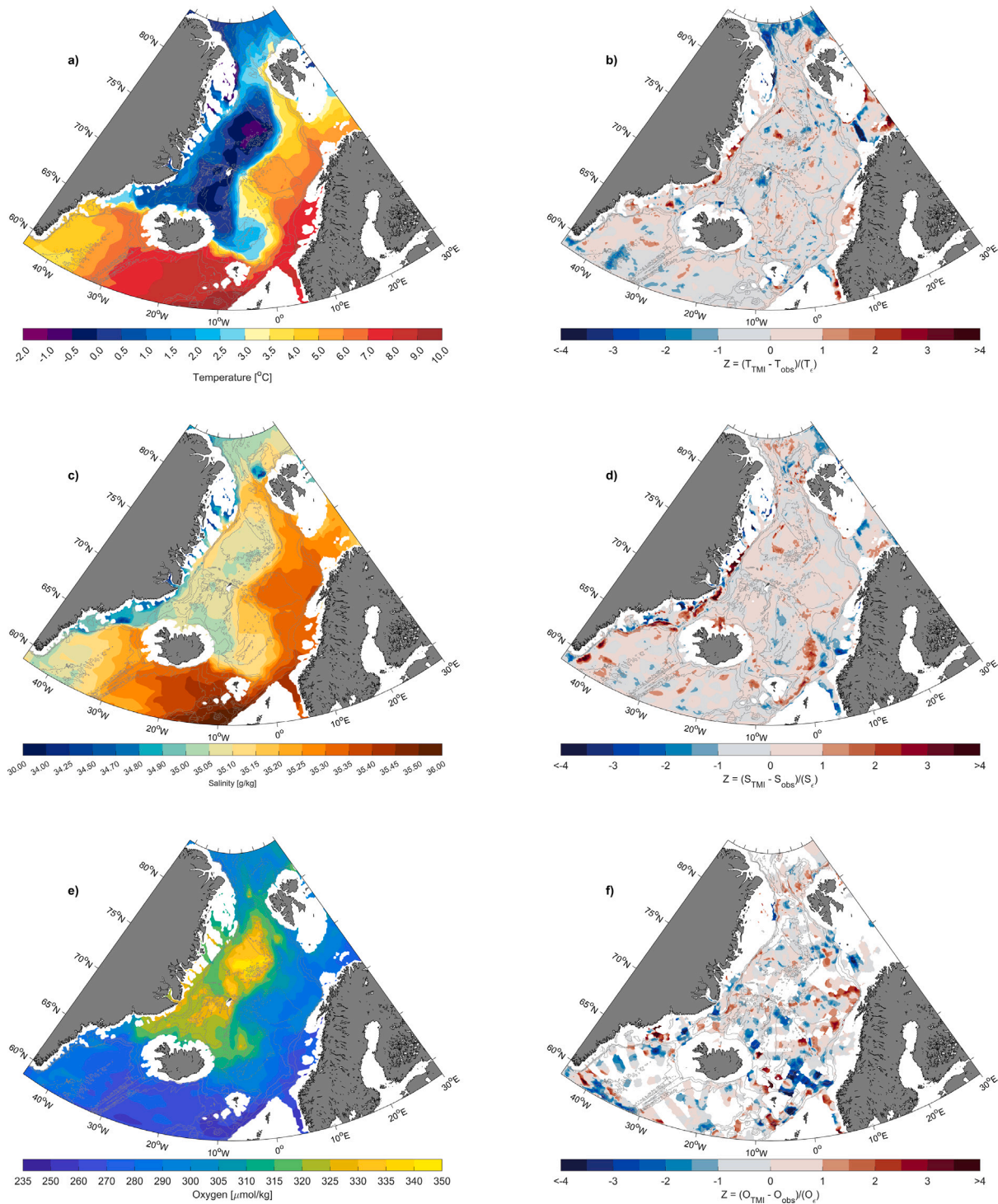
Fig. 3. Distribution of TMI temperature (T), salinity (S), and oxygen (O) at 250 m depth (left panels). The corresponding Z-score distribution for each parameter is shown in the panels to the right. The Z-score is defined as the difference between the inversion and observations divided by the observational uncertainty (ε). Positive values indicate that the TMI property is larger than the observed, while values between ±1 indicate that the difference is smaller than the uncertainty. The 500-, 1000-, 1500-, and 3000-m isobaths are shown as thin gray contours.

Instead we combine Eqs. (2) and (3) following Gebbie and Huybers (2011) such that:

$$\frac{\partial V}{\partial b} = A^{-T} v, \qquad (4)$$

which can be solved in one operation by calculating the inverse transpose of A. The partial derivative on the left side of Eq. (4) is a vector that describes the sensitivity of V to changes in the boundary conditions b. At the surface and lateral boundaries the sensitivity vector equals the volume of overflow water originating from each boundary location, while the interior values of $\partial V / \partial b$ give information about the pathways (i.e., the amount of overflow water that has passed through each interior location).
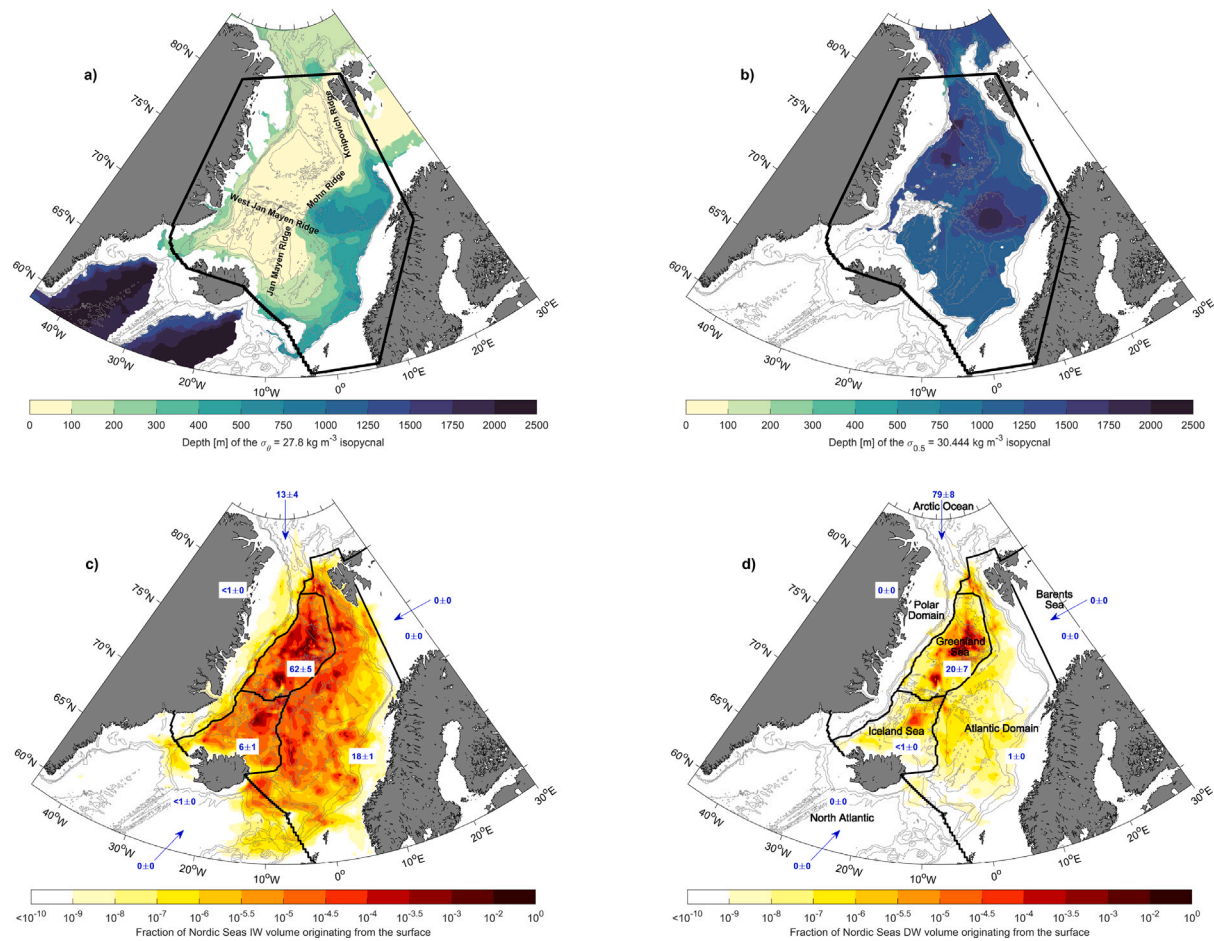
Fig. 4. Depths of the $\sigma_\Theta = 27.8$ kg m^{-3} (a) and $\sigma_{0.5} = 30.444$ kg m^{-3} (b) isopycnals. The lower panels show the fraction of contribution from the surface to the intermediate (c) and deep (d) water inventories in the Nordic Seas (defined as the region within the black contour marked in a and b). Note that the color scale is logarithmic, with dark red colors indicating substantial contributions. The blue numbers are the total contribution (in percent) from each surface region outlined in black and the lateral boundaries, and the uncertainty represents the sensitivity to the first guess of **A** (Section 3.2). The 500-, 1000-, 1500-, and 3000-m isobaths are shown as thin gray contours.

Note that the terms *origin* and *source* refer to the surface locations where the water masses constituting the overflow plumes were last in contact with the atmosphere (or the lateral boundaries if the water-masses originate outside of the domain), which is not necessarily where the largest buoyancy loss occurs (Isachsen et al., 2007).

3.5. Evaluation of the Nordic Seas TMI solution

One way to quantify how well the steady-state pathways fit the observations is to compare the TMI and observed property distributions. By construction the fields should compare well, which is evident from the vertical distribution of the average misfit for each parameter (Fig. C.1). The magnitudes of the misfits are generally similar to (or below) the observational uncertainty. The misfits also have the same vertical shape, with the largest values in the upper 500 m.

The horizontal distributions of TMI temperature, salinity, and oxygen at 250 m depth are shown in Fig. 3 along with the corresponding misfits divided by the observational uncertainty (called Z-score, e.g., Glover et al., 2011). As expected, the differences between the inversion and observations are low. The Norwegian Sea is dominated by warm and saline AW with relatively low oxygen concentration, while the Iceland and Greenland Seas are cold, oxygen-rich, with intermediate salinity. Also visible are the temperature and salinity local maxima of the Atlantic-origin water in the East Greenland Current flowing southwards along the Greenland shelf break. The TMI fields are generally smoother than the observations, which results in a patchy structure of the Z-scores. Apart from these small-scale discrepancies, the majority of the misfits are within the observational uncertainty (i.e., 82% of all Z-scores are between ±1, which indicates a slight overfit relative to the expected 67%).

4. Dense-water formation in the Nordic Seas

Before we investigate the origin and pathways of the overflow water at the GSR, we identified all areas that supply dense water to the Nordic Seas and their relative contributions. This was done by backtracking all intermediate and deep water masses within the Nordic Seas (thick black contour, Figs. 4a and b) to the surface and lateral boundaries (Section 3.4). Intermediate waters (IW) have potential densities between $\sigma_\Theta = 27.8$ kg m^{-3} and $\sigma_{0.5} = 30.444$ kg m^{-3}, while deep water (DW) is denser than $\sigma_{0.5} = 30.444$ kg m^{-3} (Rudels et al., 2005; Jeansson et al., 2008).

The upper 1500 m of the Nordic Seas water column are dominated by IW (Figs. 4a and b), in particular the western and northern areas where the IW extends to the surface during winter. These areas also supply most of the Nordic Seas IW inventory (Fig. 4c). The colors in Fig. 4c show the fraction of IW volume originating from each surface grid point. All volume fractions (including those from the lateral boundaries, not shown) add up to 1. The blue numbers on the figures indicate the total contribution (in percent) from the different source regions outlined in black and the lateral boundaries. These regions were defined based on bathymetry and surface hydrography as described below, and are used throughout the paper for easier interpretation and comparison with earlier studies.

Approximately $6 \pm 1\%$ and $62 \pm 5\%$ of the IW volume originate in the Iceland and Greenland Seas, respectively. These surface source regions are separated from the Polar Domain by the Polar Front (defined by the 34.66 g kg^{-1} surface isohaline, which corresponds to the practical salinity contour 34.50 used by Swift and Aagaard, 1981) and from the Atlantic Domain by the Arctic Front (here defined by the $2\,°C$ surface isotherm, which closely follows the Jan Mayen, Mohn, and Knipovich Ridges, Fig. 4a). The West Jan Mayen Ridge separates the Greenland and Iceland Seas. The North Atlantic is the source region south of the GSR, including the southern lateral boundary, while the Barents Sea is the region south of Svalbard and east of 19°E (which is the approximate longitude of the Barents Sea Opening transect, O'Dwyer et al., 2001). Because water modified in the Barents Sea largely continues into the Arctic Ocean before returning southwards through Fram Strait, water that was last at the surface in this area is accounted for in the inversion as a contribution from the northern lateral boundary along with other water masses flowing southwards from the Arctic Ocean. Combined, all water masses present at the northern lateral boundary, hereafter referred to as the Arctic Ocean, supply $13 \pm 4\%$ of the IW in the Nordic Seas. The remaining main contributor is the Atlantic Domain which accounts for approximately $18 \pm 1\%$.

The majority of the Nordic Seas DW stems from the Arctic Ocean ($79 \pm 8\%$, Fig. 4d). As the only source region where observations show densities greater than $\sigma_{0.5} = 30.444$ kg m^{-3} in the 2000–2019 period this was an expected result. However, the inversion also backtracks a substantial portion ($20 \pm 7\%$) of the DW to the Greenland Sea. The Nordic Seas DW is a mixture of DW formed in the Greenland Sea and the Arctic Ocean (Swift and Koltermann, 1988), but GSDW was not formed during the 2000–2019 period (e.g., Brakstad et al., 2019). To resolve the properties of the remaining GSDW at depth the inversion requires a surface contribution from the Greenland Sea. The impact of this modification on the DSOW (Section 5) is small, as only $6 \pm 2\%$ of the DSOW is supplied by DW ($4 \pm 1\%$ from the Greenland Sea and $2 \pm 1\%$ from the Arctic Ocean). Approximately $28 \pm 17\%$ of the FBCOW is supplied by DW from the Greenland Sea ($3 \pm 8\%$) and Arctic Ocean ($25 \pm 9\%$). These contributions will be discussed further in Section 6.

5. Origin and pathways of Denmark Strait Overflow Water

The hydrographic and geochemical properties in the inversion, and the corresponding Z-scores, across Denmark Strait are shown in Fig. 5. The overall distributions are well reproduced by the inversion, with the warm and saline North Icelandic Irminger Current on the Icelandic side of the strait and the cold and fresh PSW in the East Greenland Current on the Greenland side. The location as well as the properties of the DSOW plume (defined as water denser than $\sigma_\Theta = 27.8$ kg m^{-3}) are in good agreement with observations, with the exceptions of small negative biases in salinity and oxygen (Figs. 5d and f). At the interface between the overflow plume and the North Icelandic Irminger Current there is also a negative bias in both oxygen and nitrate (Fig. 5f and h, respectively), which suggests that the stoichiometric ratio may not be locally correct. This ratio is, however, known to vary spatially (Anderson and Sarmiento, 1994; Frigstad et al., 2014; Jeansson et al., 2015). We also note that large variability in DSOW volume transport and hydrographic properties are observed on short time scales (e.g., Jochumsen et al., 2017; Mastropole et al., 2017).

The origin of the DSOW plume was determined by backtracking all of the overflow water at Denmark Strait to the surface and lateral boundaries (Section 3.4). This reveals that most of the DSOW is produced in the Nordic Seas, with the largest contributions from the Greenland Sea ($39 \pm 2\%$), the Iceland Sea ($20 \pm 3\%$), and the Atlantic Domain ($19 \pm 2\%$, Fig. 6). The contribution from the Atlantic Domain stems almost entirely from the northern part near Fram Strait, in the West Spitsbergen Current. This is where the Atlantic-origin water has cooled sufficiently to leave the surface and flows beneath the fresh

PSW (Mauritzen, 1996). Most of the water from the Greenland Sea originates in the central basin, within the cyclonic gyre where the deepest convection is found (Fig. B.1, Brakstad et al., 2019). The deepest and densest convection in the Iceland Sea occurs in the north-western part, outside of the gyre (Våge et al., 2015), which also corresponds well with the elevated contributions to the DSOW (Fig. 6). The Polar Domain, mainly the region near the Polar Front, supplies $7 \pm 0\%$, while only $2 \pm 1\%$ originates in the Arctic Ocean. We also find a $12 \pm 1\%$ contribution from the North Atlantic, mainly from the region just south of Denmark Strait, which corroborates the numerical results of Saberi et al. (2020), although their simulated contribution was slightly higher (16%).

The hydrographic and geochemical properties at the boundary locations with significant DSOW contributions (fractions greater than $10^{-4.5}$, Fig. 6) vary substantially, even within each source region (Fig. 7). Hence, direct comparisons with results from earlier end-member analyses, which are sensitive to the predefined end-members, are not straightforward. One example is the temperature limit ($0\,°C$) used to separate Atlantic- from Arctic-origin waters (e.g., Rudels et al., 2005; Jeansson et al., 2008; Våge et al., 2011; Mastropole et al., 2017). Arctic-origin water masses, interpreted as IW originating in the Iceland and Greenland Seas, are typically defined as water colder than $0\,°C$. From Fig. 7a we see that IW warmer than $0\,°C$ in the Iceland and Greenland Seas contribute to the DSOW, at least based on the 2000–2019 late-winter conditions. Distinguishing Arctic- and Atlantic-origin waters by the $0\,°C$ limit would thus lead to an overestimate of water originating from the Atlantic Domain and an underestimate of water from the Iceland (in particular) and Greenland Seas.

In accordance with Våge et al. (2022), we find that most of the water formed in the Iceland Sea in the 2000–2019 period was warmer than $0\,°C$. We note that the warmest source water from the Iceland Sea ($>3\,°C$, Fig. 7a) stems from the North Icelandic Irminger Current on the shelf northwest of Iceland. Garcia-Quintana et al. (2021) suggested, based on numerical simulations, that dense-water formation on the north-west Iceland shelf can supply up to 21% of the overflow water transported by the NIJ to Denmark Strait. This is incongruent with observations, which indicate that formation of overflow water on the shelf north of Iceland is rare (Semper et al., 2022). Our inversion confirms that result, we find that the total contribution from the north Iceland shelf to the DSOW is less than 1%. Larger contributions are found from the Iceland shelf south of Denmark Strait (within the North Atlantic domain, Fig. 6), but this water recirculates in and just north of Denmark Strait and does not supply the NIJ (Saberi et al., 2020; Garcia-Quintana et al., 2021).

Another instance where comparisons between end-member analyses may be challenging is that water originating in the Greenland Sea and the Arctic Ocean can have the same hydrographic properties, while their geochemical properties differ (Fig. 7). Dense waters formed in the Greenland Sea typically have higher oxygen and lower nitrate and phosphate concentrations, because they were ventilated more recently. Hence, only studies that include geochemical parameters can distinguish water masses originating in the Arctic Ocean and in the Greenland Sea. As a result, DSOW end-member analyses solely based on hydrographic properties typically have a higher contribution from the Iceland and Greenland Seas (e.g., Mastropole et al., 2017; Lin et al., 2020), while studies also including geochemical properties often have substantial contributions from the Arctic Ocean (e.g., Tanhua et al., 2005; Jeansson et al., 2008). The TMI solution is based on hydrographic as well as geochemical observations, yet our estimated contribution from the Arctic Ocean to the DSOW is much lower than suggested by Tanhua et al. (2005) and Jeansson et al. (2008). Our contribution from the Arctic Ocean is mainly classified as deep water, while Tanhua et al. (2005) and Jeansson et al. (2008) also found a large intermediate-water contribution. The TMI source properties available at the northern lateral boundary (i.e., the Arctic Ocean, Fig. 7) are slightly more saline compared to the source properties used by Jeansson et al. (2008).
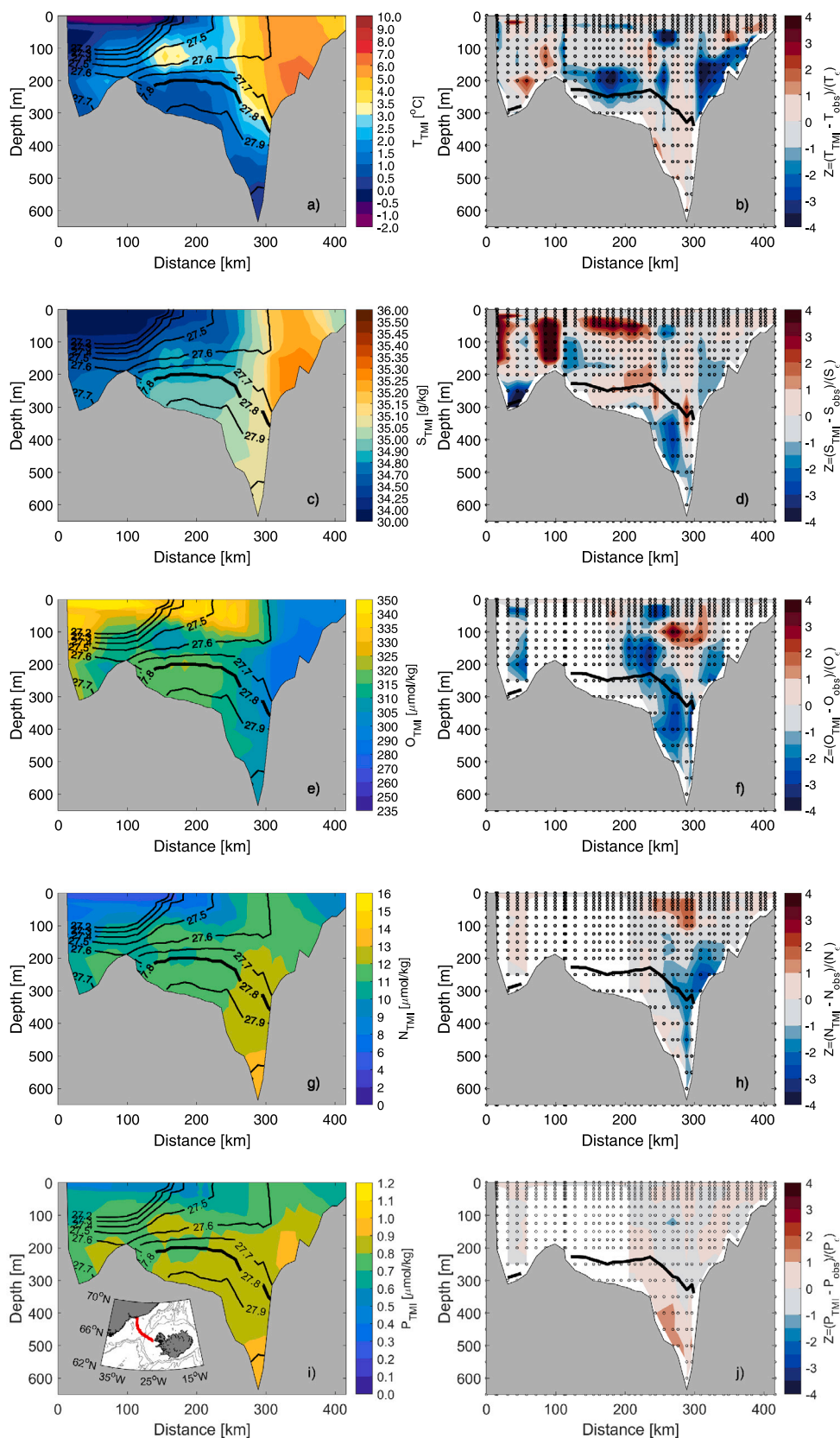
Fig. 5. TMI temperature (T), salinity (S), oxygen (O), nitrate (N), and phosphate (P) across Denmark Strait (left panels, the location of the section is indicated in red on the map inserted in panel i). The black contours show the potential density (σ_Θ) field and the thick black line marks the $\sigma_\Theta = 27.8$ kg m^{-3} isopycnal, which is the lower density limit of the overflow water. The corresponding observed overflow water limit is marked in the right panels along with the Z-score (Fig. 3) for each parameter. The TMI resolution is indicated by black circles. The x-axes show the distance along the section starting from Greenland.
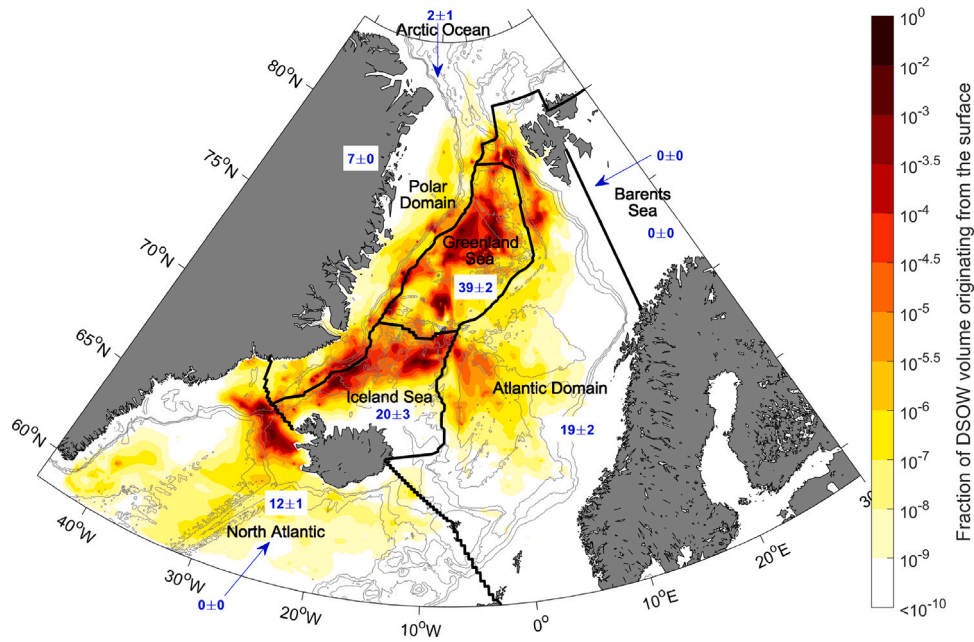
Fig. 6. Fraction of contribution from the surface to the Denmark Strait Overflow Water. Note that the color scale is logarithmic. The blue numbers indicate the total contribution (in percent) from each surface region outlined in black and the lateral boundaries, and the uncertainty represents the sensitivity to the first guess of **A** (Section 3.2). The 500-, 1000-, 1500-, and 3000-m isobaths are shown as thin gray contours.
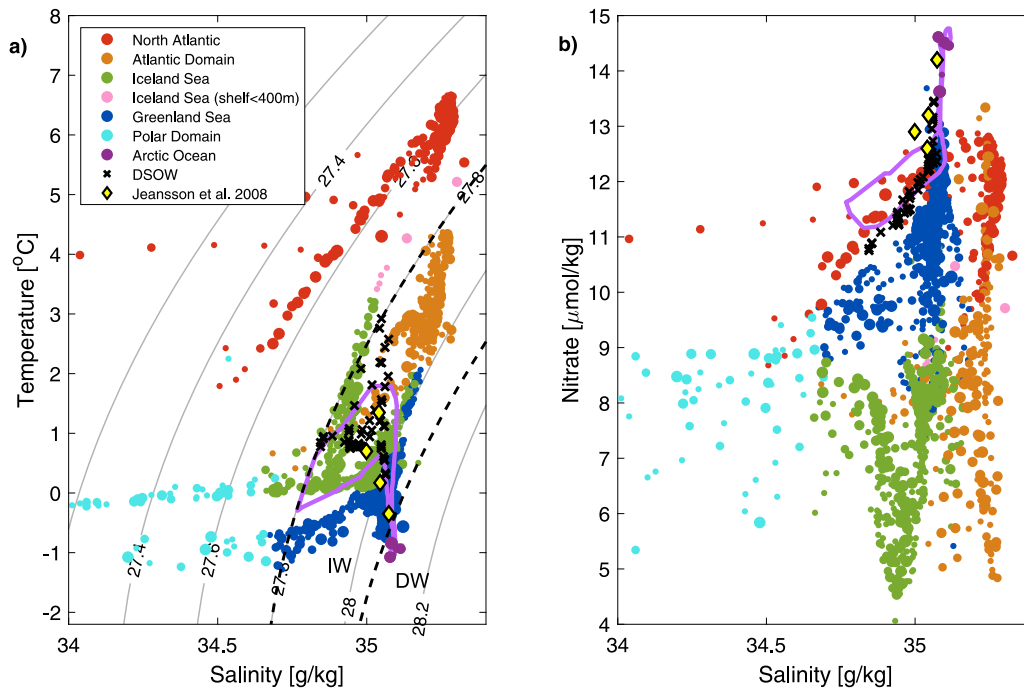
Fig. 7. Temperature and salinity (a), as well as nitrate (b) of the DSOW (black crosses) and the source regions with fractional contributions exceeding $10^{-4.5}$ (Fig. 6). The source properties (circles) are color-coded by region, while the marker sizes are scaled by the magnitude of the contribution. The purple contour outlines all properties denser than σ_Θ = 27.8 kg m^{-3} that are present at the northern lateral boundary (i.e., Arctic Ocean), while the yellow diamonds show the source properties of the intermediate water from the Arctic Ocean as defined by Jeansson et al. (2008). The gray contours in (a) indicate potential density (σ_Θ, kg m^{-3}), and the black dashed lines mark the σ_Θ = 27.8 kg m^{-3} and $\sigma_{0.5}$ = 30.444 kg m^{-3} isopycnals.

The Atlantic-origin water (>0 °C) that has encircled the Arctic Ocean also has lower nitrate concentrations (compare the purple contour and yellow diamonds in Fig. 7). This could be due to temporal variability in the water masses, which is not properly accounted for in Tanhua et al. (2005) and Jeansson et al. (2008), as their estimates are based on observations from single cruises, nor in the TMI solution, which is based on the 2000–2019 winter-mean conditions.

Although the DSOW source properties vary substantially, they form separate clusters with nearly distinct hydrographic and geochemical properties when grouped geographically (Fig. 7). Each source region
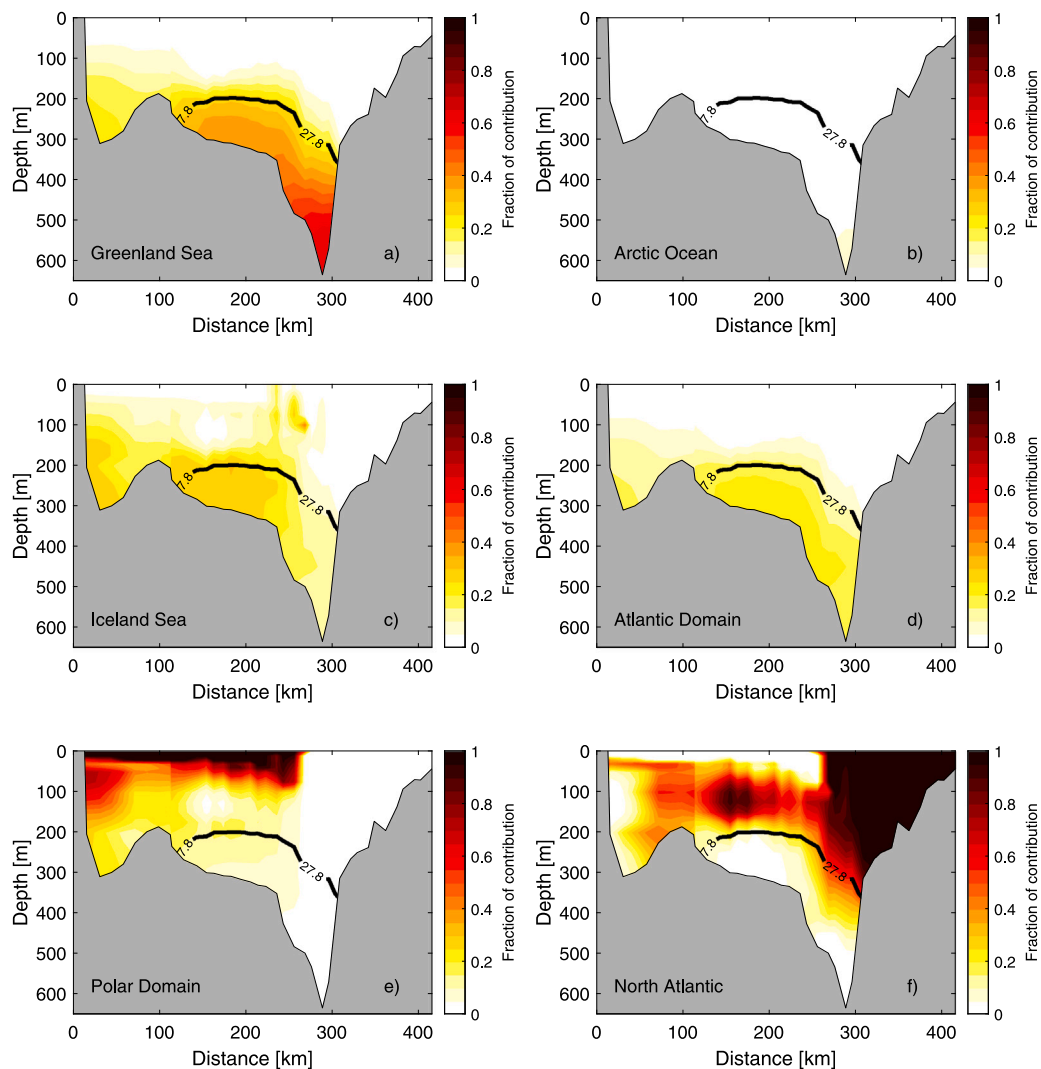
Fig. 8. Contributions from six different source regions to the transect across Denmark Strait (Fig. 5i). The lower density limit of the DSOW is indicated by the $\sigma_\Theta = 27.8$ kg m^{-3} isopycnal (black contour). The x-axes show distance along the section starting from Greenland.

also contributes to distinct parts of the DSOW plume. To investigate this further, we traced water from each boundary source region to Denmark Strait using the inverse of Eq. (2) as described in Section 3.4. The densest portion of the DSOW filling most of the deep trough is dominated by water formed in the Greenland Sea (Fig. 8a), while the Iceland Sea and the Atlantic Domain contribute to the slightly less dense components near and on the Greenland shelf break (Figs. 8c and d, respectively). This distribution is in good agreement with previous studies (Mastropole et al., 2017; Lin et al., 2020). The small contribution from the Arctic Ocean (Fig. 8b) is primarily to the densest component of the DSOW, coinciding with elevated values of nitrate and phosphate (Fig. 5g and i). As Mastropole et al. (2017) and Lin et al. (2020), we find that the Polar Domain and the North Atlantic (via the North Icelandic Irminger Current) contribute to the lightest components of the DSOW plume (Figs. 8e and f). Some of the warm water from the North Atlantic recirculates north of Denmark Strait (Casanova-Masjoan et al., 2020), but most of this water is too light to supply the overflow plume (Fig. 8f).

A major advantage of the TMI method is the possibility to identify interior pathways (Section 3.4). By backtracking overflow water from the Denmark Strait sill, we can estimate the fraction of DSOW that passed through each interior grid cell upstream of the sill (Fig. 9). The most prominent pathway is the East Greenland Current along the Greenland shelf break, which can be traced back to Fram Strait where

most of the Atlantic-origin water transported by the current was last in contact with the atmosphere (Fig. 6). Another pathway, parallel to the East Greenland Current, traces DSOW back to the central Greenland Sea. The core of the pathway is centered at 550 m depth and located roughly 70 to 120 km offshore of the Greenland shelf break. The depth and location of this pathway coincide with the deep part of the outer East Greenland Current branch that Håvik et al. (2017) observed north of the West Jan Mayen Ridge near 71°N. As Håvik et al. (2017), we cannot identify a distinct outer branch south of this ridge, where the branch appears to have merged with the shelf break branch of the East Greenland Current. The NIJ flowing along the slope north of Iceland (e.g., Semper et al., 2019), is visible only to the west of Kolbeinsey Ridge in Fig. 9. From this figure the origin of the NIJ is unclear, this will be investigated further in the following sections.

The NIJ was further examined at the Hornbanki transect upstream of Denmark Strait, corresponding to the location of one of the regular hydrographic monitoring transects north of Iceland (Jónsson and Valdimarsson, 2012; Semper et al., 2019), where the overflow water in the NIJ can be readily separated from the overflow water transported by the East Greenland Current. The section (indicated in blue in Fig. 9) was extended northward across Blosseville Basin, for complete coverage between the Iceland and Greenland shelves. The temperature and fraction of DSOW volume that has passed through the extended Hornbanki section are shown in Figs. 10a and b, respectively. From the fraction
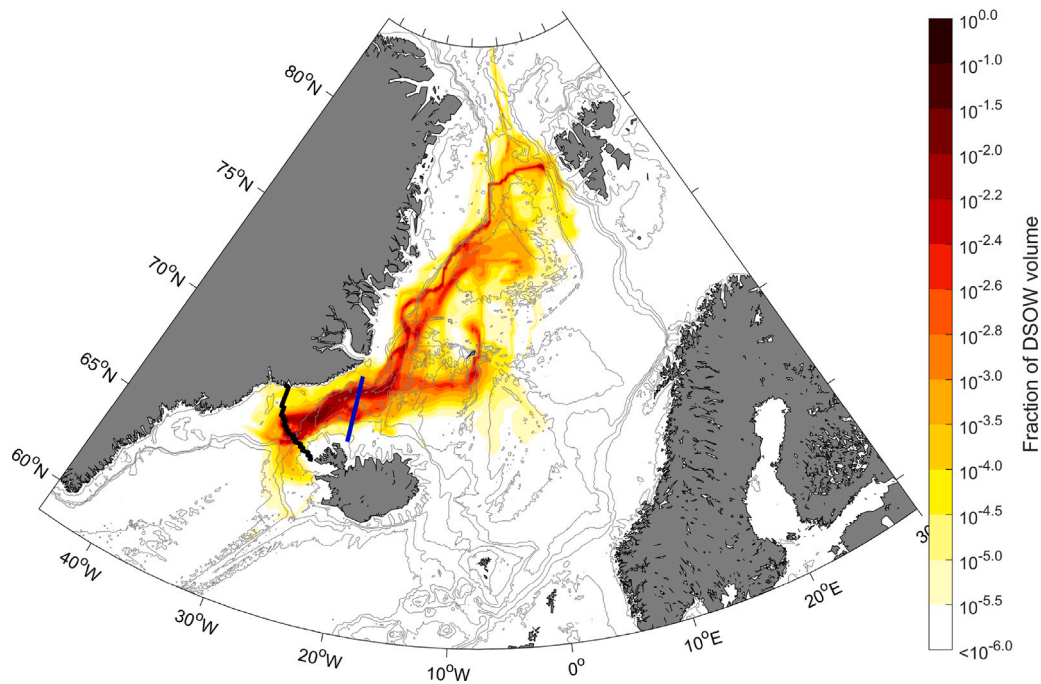
Fig. 9. Fraction of Denmark Strait Overflow Water that has passed through each horizontal location, integrated over the entire water column. Note that the color scale is logarithmic. The location of the Denmark Strait section is indicated in black, while the location of the extended Hornbanki section is marked in blue. The 500-, 1000-, 1500-, and 3000-m isobaths are shown as thin gray contours.

of DSOW volume (Fig. 10b), we identified three major local maxima that correspond to the NIJ and the separated and shelf break branches of the East Greenland Current (Våge et al., 2013; Harden et al., 2016; Semper et al., 2019). The NIJ is located between the 550 and 850 m isobaths, and is associated with a tongue of cold, dense water sloping up towards Iceland (Semper et al., 2019).

The origin and upstream pathways of the DSOW in the NIJ (black circles, Fig. 10b) are shown in Fig. 11. In accordance with Huang et al. (2020), we find that most of the overflow water in the NIJ originates in the Greenland Sea (82 ± 2%), while the remaining portion is supplied by the Arctic Ocean (8 ± 2%), the Iceland Sea (5 ± 1%), and the Atlantic Domain (5 ± 1%). The water originating in the Greenland Sea follows two main pathways towards Denmark Strait. One is the outer core of the East Greenland Current (Håvik et al., 2017), which is supported by RAFOS float tracks (de Jong et al., 2018) and an SF_6 tracer release experiment (Messias et al., 2008), but not among the pathways suggested by Huang et al. (2020). Based on hydrographic observations and surface geostrophic velocities from satellite, Huang et al. (2020) found two branches of dense water flowing southward along the submarine ridges surrounding the central Iceland Sea: one current east of the Kolbeinsey Ridge and another east of the Jan Mayen Ridge. Our inversion suggests that the southward flow along the Jan Mayen Ridge primarily supplies overflow water to the Faroe Bank Channel (Section 6), while the southward flow along the eastern side of the Kolbeinsey Ridge could be represented by our other main pathway from the Greenland Sea (Fig. 11). Following this pathway, dense water formed in the Greenland Sea flows through the Jan Mayen Channel in the Mohn Ridge, then enters the Iceland Sea across the sloping Jan Mayen Ridge just south of Jan Mayen. Across the ridge, the pathway is centered between the 400 and 600 m isobaths and associated with upsloping isopycnals similar to the NIJ along the slope north of Iceland (not shown). Observations on the Jan Mayen Ridge are sparse, but two years (2007–2009) of moored measurements from the 800 m isobath indicate a consistent westward flow across the ridge below 300 m depth (Mork et al., 2014a). The average westward velocity (increasing with depth to about 1.2 cm s^{-1} near the bottom) was relatively weak,

but the location of the mooring was on the outskirts of the pathway identified by the inversion, where the slope along the crest of the ridge is substantially reduced. Within the Iceland Sea the water follows the cyclonic gyre circulation, which leads to a southward flow east of the Kolbeinsey Ridge. The majority of the water crosses the Kolbeinsey Ridge near the Spar Fracture Zone at depths of 400–800 m and feeds the NIJ as it progresses westward along the Iceland slope from northeast of Iceland to Denmark Strait.

The origin of the shelf break and separated branches of the East Greenland Current (dark and light blue circles, Fig. 10b) were also determined similar to the NIJ. Combined, 20 ± 1% of the overflow water from the EGC system at Hornbanki stems from the Atlantic Domain, while the Greenland and Iceland Seas account for 50 ± 2% and 26 ± 6%, respectively (not shown). This indicates that substantial mixing occurs between the East Greenland Current and the interior basins (Strass et al., 1993; Rudels et al., 2002; Jeansson et al., 2008; Håvik et al., 2019) or that the current is directly ventilated along the pathway (Våge et al., 2018; Moore et al., 2022; Våge et al., 2022). To investigate where the mixing takes place we applied a dye to the northern part of the Atlantic Domain and quantified how the dye was diluted from Fram Strait to Denmark Strait (Fig. 12). At each latitude, we identified the core of the Atlantic-origin water in the East Greenland Current by Atlantic Domain contributions ≥25%. Grid cells satisfying this criterion coincided with the subsurface temperature and salinity maxima in the current as illustrated at the extended Hornbanki section (Fig. 10a). The mean contribution from the Atlantic Domain to this core volume, as well as the contributions from the Greenland and Iceland Seas were then estimated for each latitude (Fig. 12b). In Fram Strait, outside the Atlantic Domain, we find that approximately 60% of the East Greenland Current core volume is Atlantic-origin water. As the water progresses southwards, it is increasingly influenced by water from the interior Iceland and Greenland Seas. There are two latitude bands where substantial mixing with the interior basins and dilution of the Atlantic-origin water occur. This is in the Greenland Sea between 76°N and 75°N, and in the Iceland Sea between 69.5°N and 68.5°N, which corroborates the results of Strass et al. (1993) and Håvik
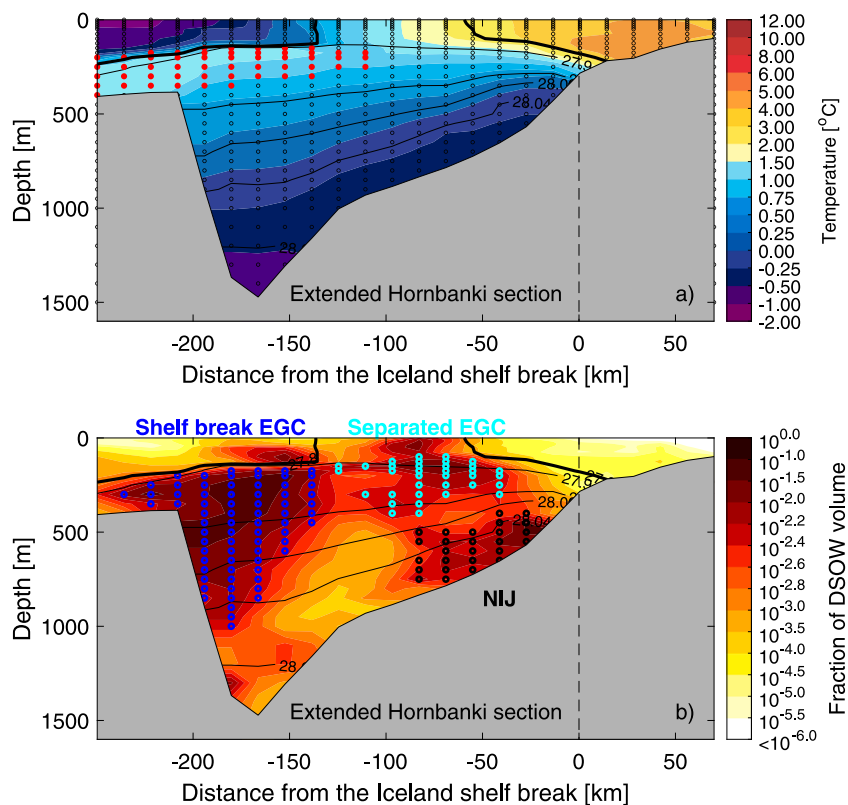
Fig. 10. Temperature (a) and fraction of DSOW volume that has passed through the extended Hornbanki section (b). The location of the section is shown in Fig. 9. The black contours show potential density (σ_Θ, kg m^{-3}). The black circles in a) indicate the TMI resolution, while the red circles mark grid cells with a large ($\geq 25\%$) contribution from the Atlantic Domain. The colored circles in b) mark grid cells identified as the NIJ (black), and as the shelf break (dark blue) and separated (light blue) East Greenland Current (EGC).
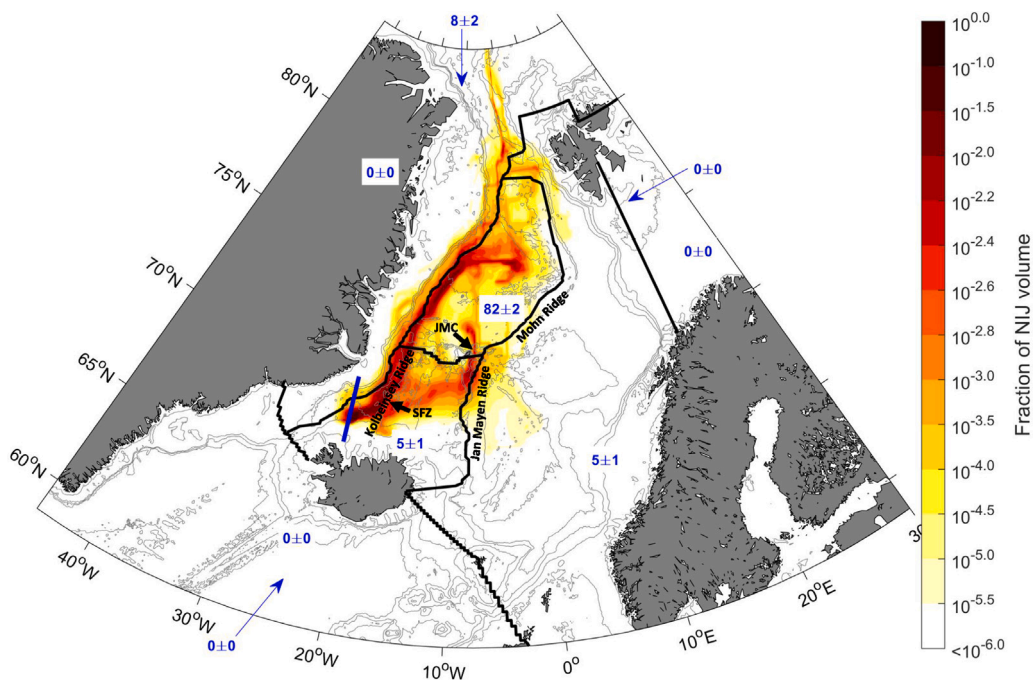
Fig. 11. Upstream pathways of the NIJ, shown as the fraction of NIJ volume that has passed through each horizontal location integrated over the entire water column. Note that the color scale is logarithmic. The blue numbers indicate the total contribution (in percent) from each surface region outlined in black and the lateral boundaries, and the uncertainty represents the sensitivity to the first guess of A (Section 3.2). The location of the extended Hornbanki section is indicated in blue, while the 500-, 1000-, 1500-, and 3000-m isobaths are shown as thin gray contours. The acronyms are: JMC=Jan Mayen Channel and SFZ=Spar Fracture Zone.
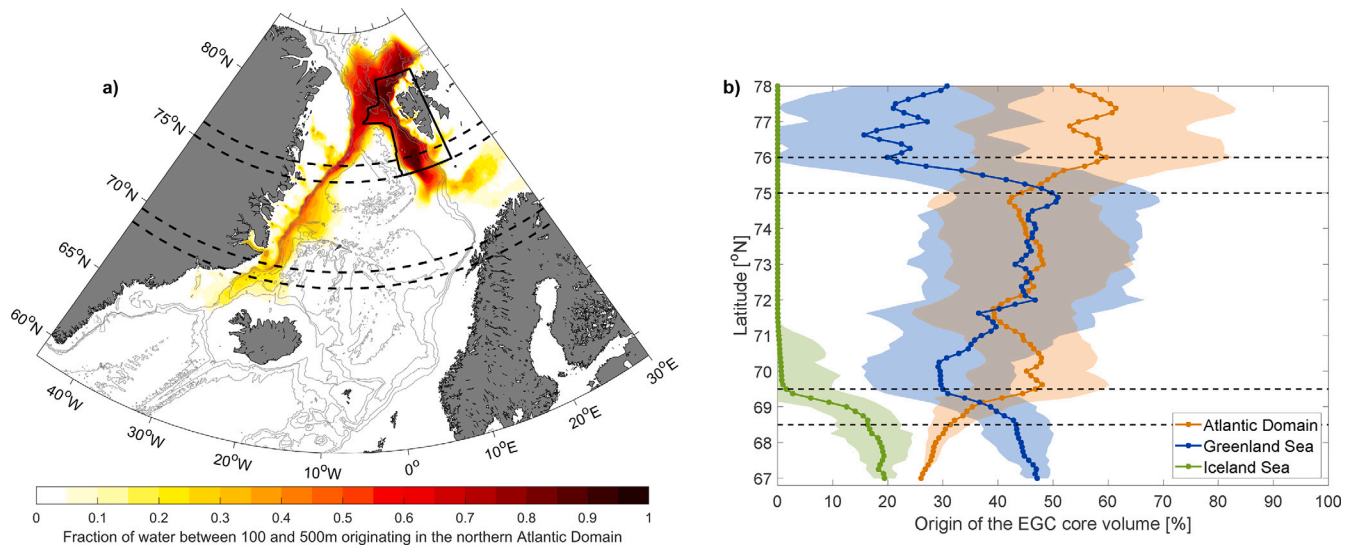
Fig. 12. Contribution from the northern part of the Atlantic Domain (solid black box) to the water column between 100 and 500 m depth (a) and along-stream contribution from the Atlantic Domain, Greenland Sea, and Iceland Sea to the East Greenland Current (EGC) core volume (b). The core volume was defined as all grid cells with ≥25% contribution from the Atlantic Domain, which overlaps with the temperature and salinity maxima in the EGC as illustrated by red circles in Fig. 10a. The colored lines and shading in b) represent the mean contribution from each source region and ±1 standard deviation. The black dashed lines in both panels mark latitude bands where the EGC experiences significant mixing with ambient water masses, which dilutes the signal from the Atlantic Domain.

et al. (2019). Associated with these regions of enhanced mixing is a decline in Atlantic-origin water temperature (approaching −0.5 °C, not shown). Håvik et al. (2019) also found a strong decline in temperature around 69°N and attributed this to a local maximum in eddy activity and the bifurcation of the East Greenland Current into the separated and shelf break branches.

6. Origin and pathways of Faroe Bank Channel Overflow Water

A similar analysis was performed to determine the origin and pathways of the overflow water in the Faroe-Shetland Channel, upstream of the Faroe Bank Channel (Fig. 1). The Faroe-Shetland Channel section was chosen because the overflow water across the section is better represented with the TMI resolution due to the larger channel width. As the overflow water in the Faroe-Shetland Channel continues downstream into the Faroe Bank Channel, we will refer to it as Faroe Bank Channel Overflow Water (FBCOW). We note that there could be a slight dense bias in the FBCOW since the Faroe-Shetland Channel is nearly 200 m deeper than the Faroe Bank sill. The hydrographic and geochemical properties across the Faroe-Shetland Channel and the corresponding Z-scores are shown in Fig. 13. Warm, saline, low-oxygen AW dominates the upper part of the water column, while the deeper parts are occupied by cold and dense ($\sigma_\Theta \geq 27.8$ kg m^{-3}) overflow water. Even though there is a positive salinity bias near the $\sigma_\Theta = 27.8$ kg m^{-3} isopycnal (Fig. 13d), the depth of the isopycnal is well captured. There are substantial biases within the overflow water, at least relative to the uncertainty associated with temporal variability in the observations. The plume is slightly warmer than observed and the oxygen, nitrate, and phosphate concentrations are too large (Fig. 13b, f, h, j, respectively). It is important to note that the uncertainty related to temporal variability is low within the overflow plume, and the average TMI-to-observational differences are only 0.11 °C, 7.38 μmol kg^{-1}, 0.42 μmol kg^{-1}, and 0.06 μmol kg^{-1} for temperature, oxygen, nitrate, and phosphate, respectively. The positive bias in both oxygen and nitrate/phosphate suggests that the stoichiometric ratio would need adjustment locally. As this is a local signal, using another stoichiometric ratio ($\Delta P : 16\Delta N : -138\Delta O$, Redfield et al., 1963) did not improve the

TMI solution. The results were similar both in terms of FBCOW biases and overflow water source contributions (not shown).

The origins of the FBCOW were determined by backtracking the overflow water in Faroe-Shetland Channel (Fig. 13) to the source regions. The contributions from the surface and lateral boundaries reveal that the two most important source regions of the FBCOW are the Greenland Sea (46 ± 8%) and the Arctic Ocean (25 ± 9%, Fig. 14). The FBCOW is denser than the DSOW (Figs. 7 and 15), hence a greater portion of the FBCOW originates in the Greenland Sea and Arctic Ocean, where the densest boundary conditions are located. Another difference between the origin of the FBCOW and the DSOW is the contribution from the Polar Domain. The majority of the fresh PSW is advected southwards by the East Greenland Current through Denmark Strait (Fig. 8e). Some of the PSW mixes with denser water and is entrained into the DSOW. Some PSW is also diverted into the interior basins of the Nordic Seas (Langehaug et al., 2022), but the amount is small and does not reach the Faroe-Shetland Channel. The Atlantic Domain accounts for 11 ± 1% of the FBCOW (Fig. 14), mainly from the southwestern part of the Norwegian Basin as suggested by Eldevik et al. (2009), while the Iceland Sea and the North Atlantic supply 10 ± 1% and 9 ± 0%, respectively.

Based on the properties at the boundary locations with significant FBCOW contributions (fractions greater than $10^{-4.5}$, Fig. 14), we find that the overflow is composed of 28 ± 1% DW, 55 ± 1% IW, while the remaining 17 ± 1% was originally less dense than $\sigma_\Theta = 27.8$ kg m^{-3} (Fig. 15). Of the DW, 3 ± 8% originates in the Greenland Sea (i.e, between 0 and 11%, as the contributions are always ≥0) and 25 ± 9% in the Arctic Ocean, while the IW contribution from the Greenland Sea and Arctic Ocean is 43 ± 0% and 0 ± 0%, respectively. Fogelqvist et al. (2003) and McKenna et al. (2016) decomposed the FBCOW into Norwegian Sea IW and DW, and found that roughly 50% of the overflow is Norwegian Sea DW (which, in turn, stems from the Greenland Sea and the Arctic Ocean, Swift and Koltermann, 1988). According to Turrell et al. (1999) and Fogelqvist et al. (2003) the DW supply has decreased due to the cessation of very deep convection in the Greenland Sea. This could be one explanation for our overall lower DW and higher IW contributions in 2000–2019, which would imply
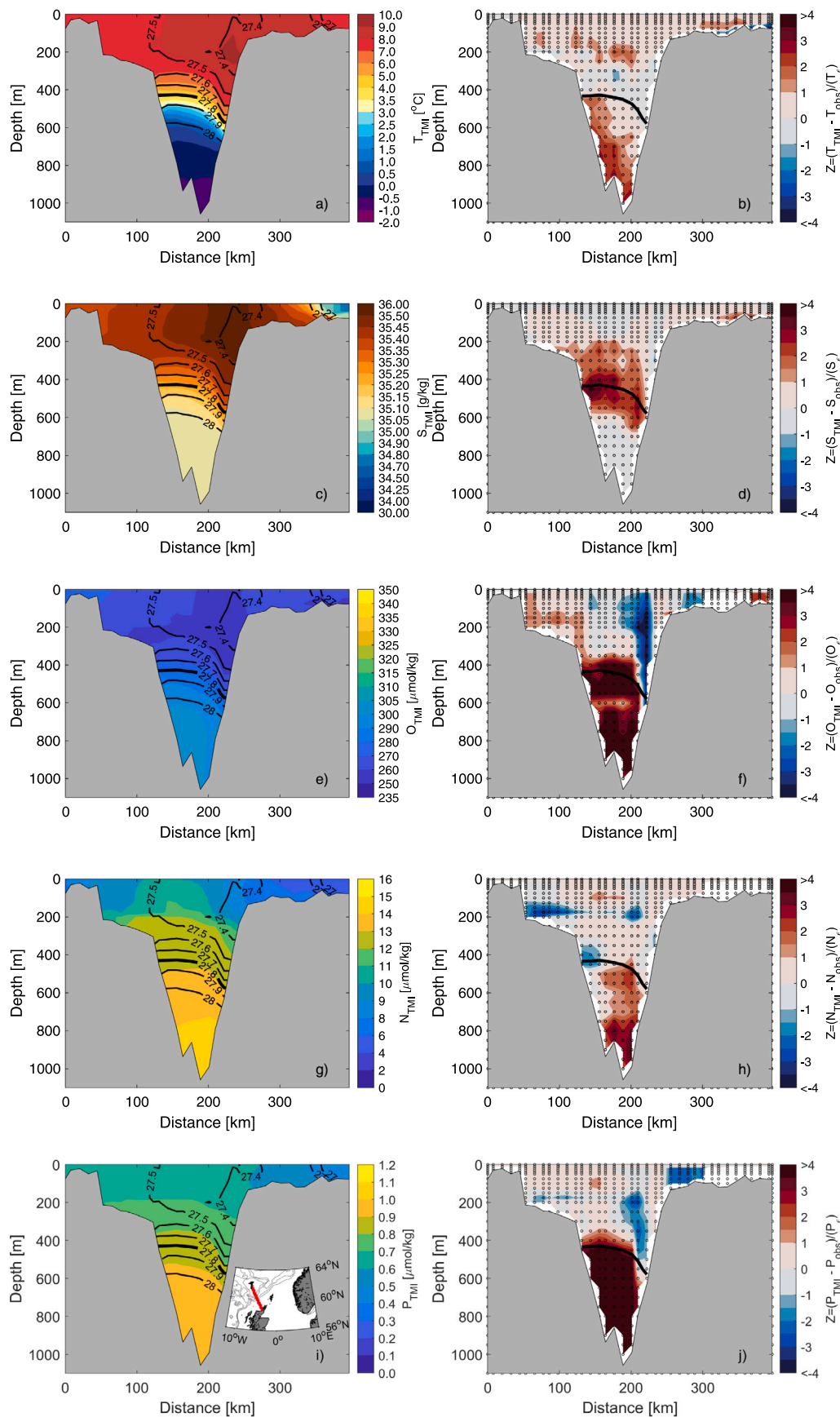
Fig. 13. TMI temperature (T), salinity (S), oxygen (O), nitrate (N), and phosphate (P) across the Faroe-Shetland Channel (left panels, the location of the section is indicated in red on the map inserted in panel i). The black contours show the potential density (σ_Θ) field and the thick black line marks the σ_Θ = 27.8 kg m^{-3} isopycnal, which is the lower density limit of the overflow water. The corresponding observed overflow water limit is marked in the right panels along with the Z-score (Fig. 3) for each parameter. The TMI resolution is indicated by black circles. The x-axes show the distance along the section starting from the Faroe Islands.
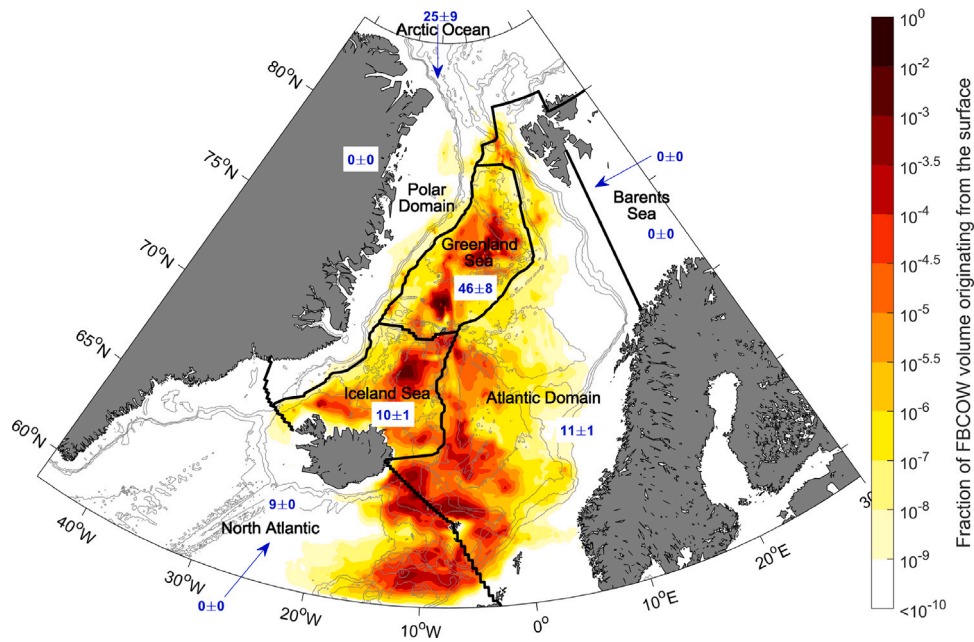
Fig. 14. Fraction of contribution from the surface to the Faroe Bank Channel Overflow Water. Note that the color scale is logarithmic. The blue numbers indicate the total contribution (in percent) from each surface region outlined in black and the lateral boundaries, and the uncertainty represents the sensitivity to the first guess of A (Section 3.2). The 500-, 1000-, 1500-, and 3000-m isobaths are shown as thin gray contours.
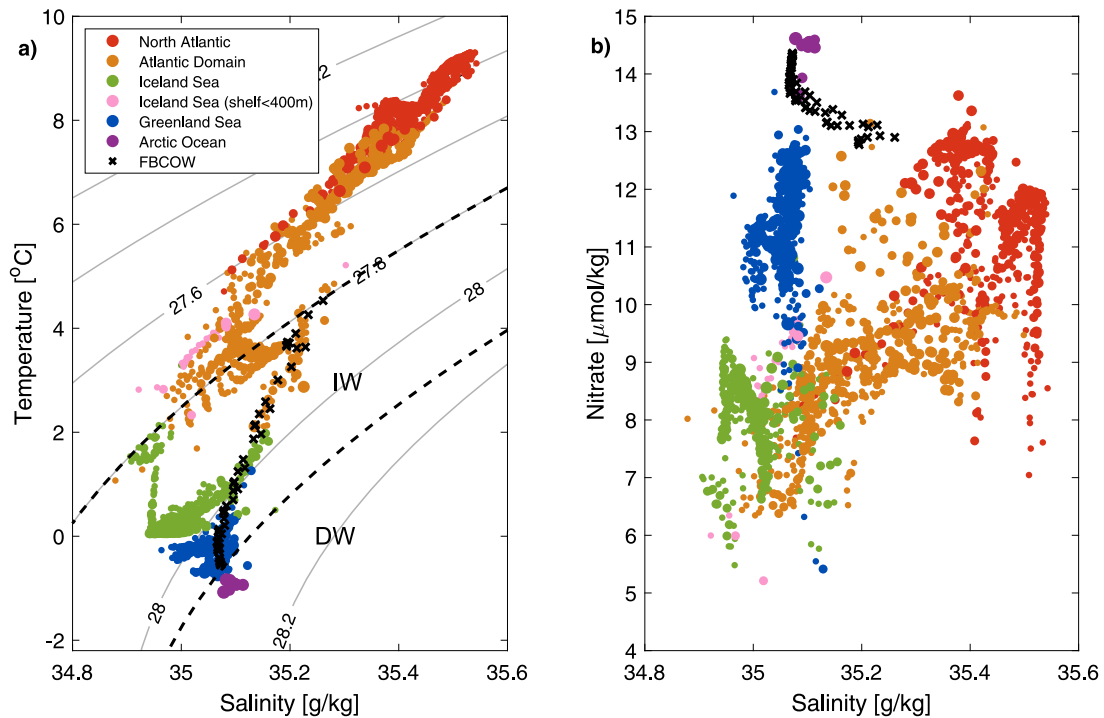

Fig. 15. Temperature and salinity (a), as well as nitrate (b) of the FBCOW (black crosses) and the source regions with fractional contributions exceeding $10^{-4.5}$ (Fig. 14). The source properties are color-coded by region, while the marker sizes are scaled by the magnitude of the contribution. The gray contours in (a) indicate potential density (σ_Θ, kg m^{-3}), and the black dashed lines mark the $\sigma_\Theta = 27.8$ kg m^{-3} and $\sigma_{0.5} = 30.444$ kg m^{-3} isopycnals.

that the entire FBCOW has become less dense. As for the DSOW, the contribution from the Arctic Ocean to the FBCOW is mainly classified as DW. This is incongruent with Jeansson et al. (2017), who determined a substantial intermediate-water contribution from the Arctic Ocean to the Norwegian Sea upstream of the Faroe-Shetland Channel.

The contribution from each geographical source region to the transect across the Faroe-Shetland Channel is shown in Fig. 16. The densest component of the overflow water is dominated by water formed in the Greenland Sea (above 40%) and the Arctic Ocean (approaching 60% in the deepest part of the trough), while the Iceland Sea and Atlantic Domain contribute to the less dense components (Fig. 16a, b,
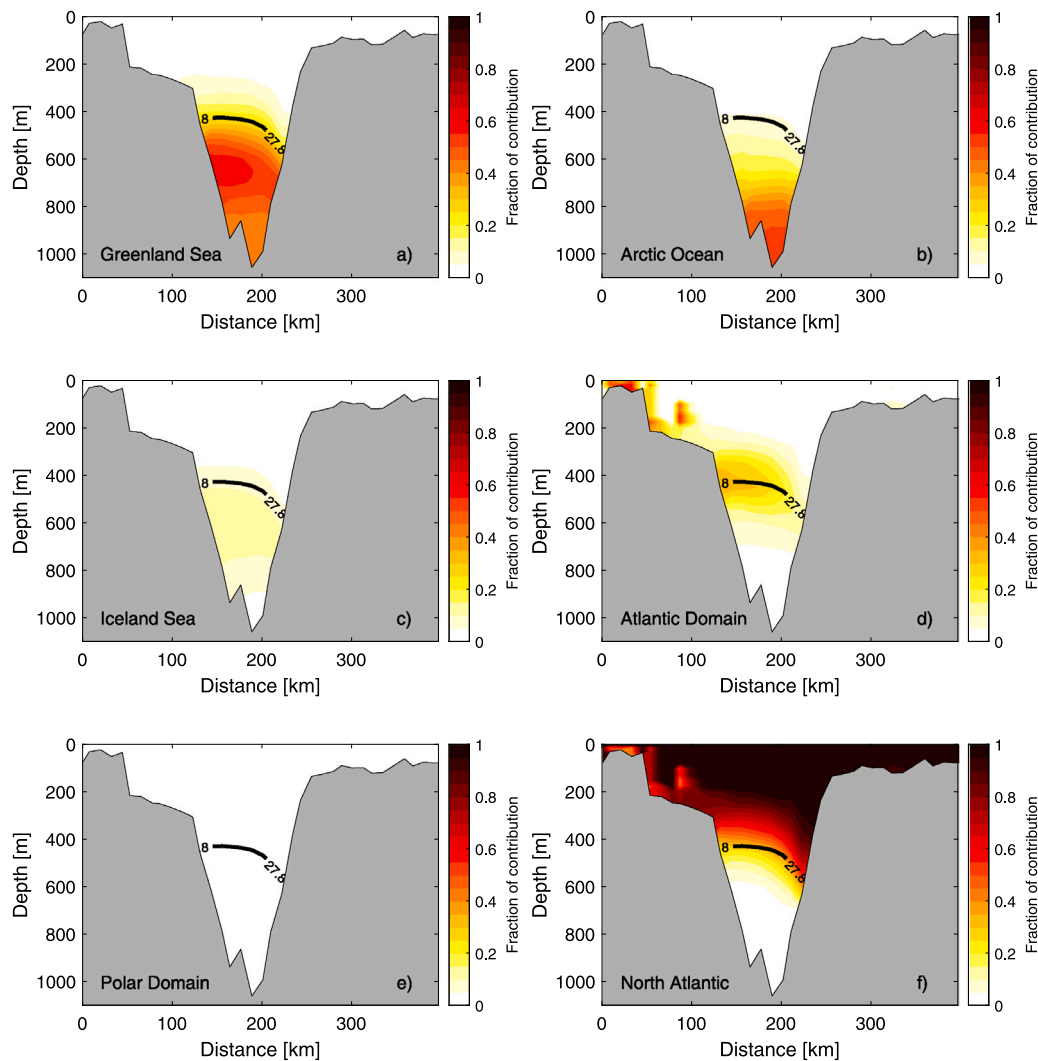
Fig. 16. Contributions from six different source regions to the transect across the Faroe-Shetland Channel (Fig. 13i). The lower density limit of the FBCOW is indicated by the σ_{Θ} = 27.8 kg m^{-3} isopycnal (black contour). The x-axes show distance along the section starting from the Faroe Islands.

c, and d, respectively). This is in agreement with Jeansson et al. (2017), who found that the primary sources of the lightest IW upstream in the Norwegian Sea were Atlantic-origin water and Arctic-origin water from the Iceland Sea, while the densest component mainly originated in the Greenland Sea and Arctic Ocean. The North Atlantic (Fig. 16f) dominates the supply of the AW in the upper part of the water column, and a small portion of this water is entrained into the overflow water.

The upstream pathways of the water masses constituting the FBCOW are visualized in Fig. 17. In accordance with Chafik et al. (2020) and Hátún et al. (2021), two main pathways of overflow water approach the Faroe-Shetland Channel, where they merge and continue toward the sill. One pathway approaches the channel from the northwest and the other from the northeast following the Norwegian continental slope. The FBCOW transported with the latter pathway also stems from the northwest farther upstream, as noted by Chafik et al. (2020). From Fig. 17 it is difficult to separate the individual pathways farther upstream. However, we can identify elevated FBCOW fractions along the GSR from northeast of Iceland toward the Faroe-Shetland Channel. This pathway corresponds to the recently documented IFSJ (Semper et al., 2020). Another major upstream pathway is visible all along the eastern side of the Jan Mayen Ridge. This is not a surprising result as

previous studies, both observational and numerical, show evidence of this southward-flowing current (e.g., Olsson et al., 2005; Voet et al., 2010; Serra et al., 2010; Köhl, 2010; Huang et al., 2020; Hátún et al., 2021). However, the contribution from this current to the FBCOW and how it connects water from the source regions to the Faroe Bank Channel are not well known.

To investigate the connection between the FBCOW, the various pathways, and the source regions, we constructed a section upstream of the Faroe-Shetland Channel (marked in blue in Fig. 17) where the two main pathways approaching the channel could easily be identified and distinguished. The fraction of FBCOW that has passed through this section is shown in Figs. 18a and b for the western and eastern legs of the section, respectively. In the western part of the section (Fig. 18a), there is a local maximum along the Faroe slope that we divided into the Faroe Current and the IFSJ by the σ_{Θ} = 27.8 kg m^{-3} isopycnal (Semper et al., 2020). The Faroe Current primarily consists of warm and saline AW from the North Atlantic (39 ± 2%) and the Atlantic Domain of the Nordic Seas (50 ± 1%), that recirculates around the Faroe Islands (Berx et al., 2013; Rossby et al., 2018). By the time this recirculating current reaches the Faroe-Shetland Channel, part of it is sufficiently dense to contribute to the lightest component of the FBCOW (Fig. 16d).
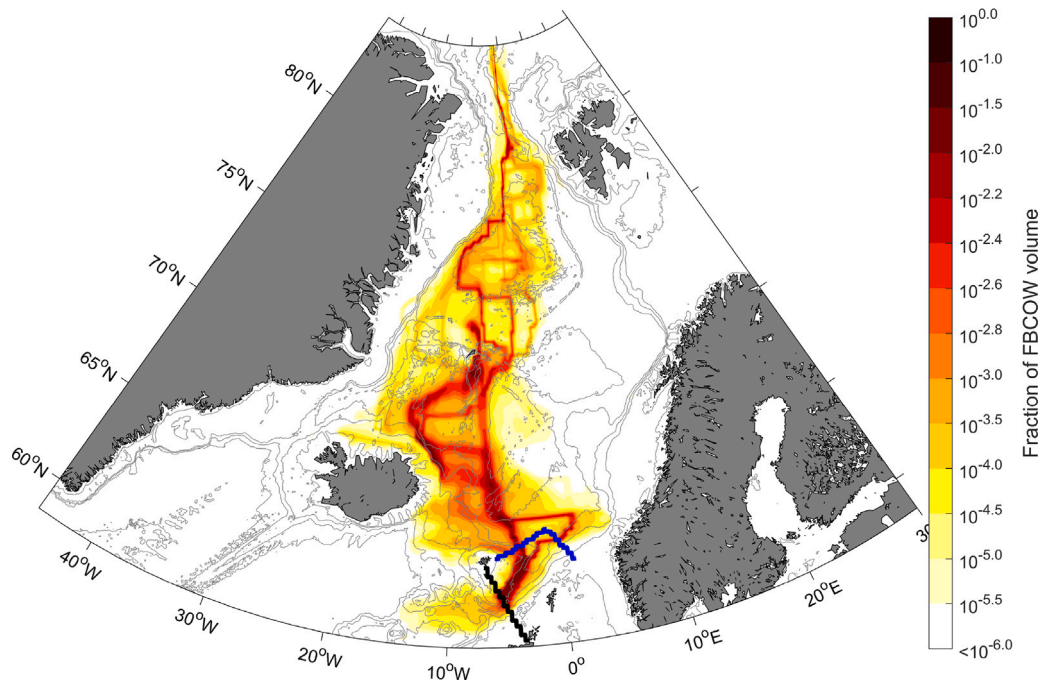
Fig. 17. Fraction of Faroe Bank Channel Overflow Water that has passed through each horizontal location, integrated over the entire water column. Note that the color scale is logarithmic. The location of the Faroe-Shetland Channel section is indicated in black, while the location of the section upstream of the Faroe-Shetland Channel is marked in blue. The 500-, 1000-, 1500-, and 3000-m isobaths are shown as thin gray contours.

The IFSJ was identified as water denser than $\sigma_\Theta = 27.8$ kg m^{-3} (Fig. 18a). The maximum associated with this FBCOW core extends down to a density of $\sigma_\Theta = 28.04$ kg m^{-3}, which is lighter than the maximum density found by Semper et al. (2020) of $\sigma_\Theta = 28.06$ kg m^{-3}. Despite the light density bias, the upstream pathway of the core (Fig. 18c) closely resembles the IFSJ. Almost half of the IFSJ volume stems from the Greenland Sea (48 ± 3%), while 11 ± 6% originates in the Arctic Ocean. Water from both of these source regions exits the Greenland Sea through gaps in the Mohn Ridge (e.g., Shao et al., 2019; Wang et al., 2021). Then the majority of the water follows a similar route as that which supplies the NIJ (i.e., across the sloping Jan Mayen Ridge between the 400 and 600 m isobaths just south of Jan Mayen, then anticlockwise around the Iceland Sea, Fig. 11). Some of the water that exits the Greenland Sea deeper in the water column continues farther south along the Jan Mayen Ridge below 1000 m depth before entering the Iceland Sea through a deep gap in the ridge (Fig. 18c). The two pathways merge along the northeast Iceland slope approximately where the NIJ emerges (Semper et al., 2019). According to Semper et al. (2022), this is a region of enhanced eddy kinetic energy, which could be linked to the emergence of the NIJ as suggested by Våge et al. (2011), as well as the separation of the NIJ and IFSJ. Downstream from the region northeast of Iceland we observe several branches exiting the Iceland Sea. Semper et al. (2020) identified two cores of the IFSJ on the slope along the GSR, but the inversion suggests that several branches also exist farther offshore in line with Argo-float trajectories (Hátún et al., 2021). Mixing with ambient water along the pathways results in a 16 ± 3% and 18 ± 1% contribution from the Iceland Sea and Atlantic Domain, respectively, while the North Atlantic contributes 7 ± 1% to the IFSJ core.

Another pronounced FBCOW core was identified on the eastern side of the section upstream of the Faroe-Shetland Channel (Fig. 18b). This core is situated deep in the water column, between 1000 and 1300 m depth, and supplies the densest component of the FBCOW (corroborating the results of Chafik et al., 2020). Nearly all of the overflow water following this pathway originates in the Arctic Ocean (62 ± 23%) and Greenland Sea (36 ± 23%). Dense water from the Arctic Ocean flows southward through Fram Strait and into the central Greenland Sea, where it continues southward across the Mohn Ridge along with water formed locally in the Greenland Sea (Fig. 18d). After exiting the Greenland Sea, the water follows the eastern side of the Jan Mayen Ridge towards the Faroe Islands, before turning eastwards with the cyclonic circulation in the Norwegian Basin (e.g., Hátún et al., 2021). When approaching the Norwegian slope and the Vøring Plateau, the overflow water is deflected south towards the Faroe-Shetland Channel. The total contribution from this deep pathway to the FBCOW was estimated to 24 ± 3%, while the IFSJ and Faroe Current account for 58 ± 3% and 18 ± 1%, respectively.

We note that several of these deep pathways appear very straight, with sharp edges (Fig. 18c). The TMI pathways are solely based on hydrographic and geochemical water-mass properties, and thus, they are not directly dynamically constrained. Weak or no gradients in water-mass properties, as typically observed at depth, may therefore result in non-physical straight pathways that sometimes cross isobaths to minimize distance. The contributions from the Greenland Sea and Arctic Ocean to the deep FBCOW pathway also have relatively high uncertainties (Fig. 18c). This is probably due to some GSDW, which was formed before the 2000–2019 period considered here, remaining at depth. As the inversion is not guided by strong data constraints to resolve this portion, the solution is more sensitive to the first guess of the pathway matrix **A** (Section 3.2).

7. Summary and conclusions

In this study we developed a regional version of the TMI inverse method to determine the origin, pathways, and final composition of the overflow water in Denmark Strait and the Faroe Bank Channel, the two main passages of dense water from the Nordic Seas to the
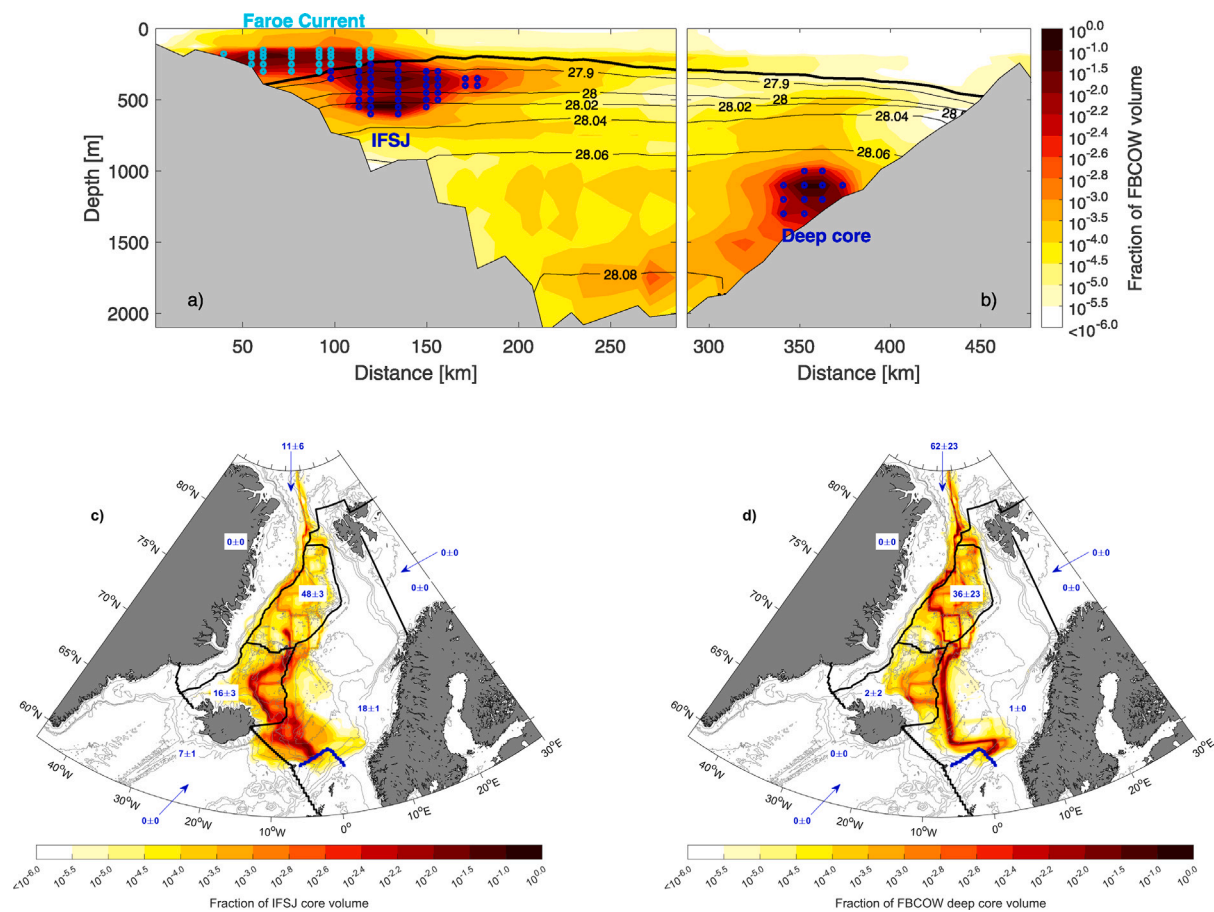
Fig. 18. Fraction of FBCOW volume that has passed through the section upstream of the Faroe-Shetland Channel (a and b). The location of the section is shown in Fig. 17. The black contours show potential density (σ_Θ, kg m^{-3}). The colored circles in a) mark grid cells identified as the Faroe Current (light blue) and IFSJ (dark blue), while the dark blue circles in b) identify a deep FBCOW core. The upstream pathways of the identified IFSJ (c) and deep core (d) are shown as the fraction of volume that has passed through each horizontal location integrated over the entire water column. Note that the scale is logarithmic. The blue numbers in c) and d) indicate the total contribution (in percent) from each surface region outlined in black and the lateral boundaries, and the uncertainty represents the sensitivity to the first guess of *A* (Section 3.2).

deep North Atlantic (Østerhus et al., 2019). The TMI method includes both hydrographic and geochemical observations, as well as their geographical distributions, which is a major advantage compared to traditional decomposition methods (e.g., Mastropole et al., 2017; Tanhua et al., 2005; Jeansson et al., 2008) as it resolves also the pathways connecting the overflow plumes to their origins. The resulting overflow water compositions are not dependent on a few pre-defined end-members, but consider all surface and lateral boundary locations as potential sources. This is crucial to determine the importance of different source regions, as water-mass properties vary spatially, also within each source region (Figs. 7 and 15). Compared to earlier global TMI versions (Gebbie and Huybers, 2010; Gebbie, 2014), the regional high-resolution inversion was able to resolve the narrow overflow water pathways and complex bathymetry of the Nordic Seas, which gave a more realistic representation of the dense-water circulation. The pathways were also improved by implementing a more realistic first guess based on density and absolute geostrophic velocity estimated from hydrographic observations and satellite altimetry.

The majority of the DSOW originates in the Greenland Sea (39 ± 2%), the Iceland Sea (20 ± 3%), and the Atlantic Domain (19 ± 2%) of the Nordic Seas. Consistent with previous studies, we find that dense water from these source regions approaches Denmark Strait in the East Greenland Current and the North Icelandic Jet (Mauritzen, 1996; Våge et al., 2011; Harden et al., 2016). The East Greenland Current

transports warm and saline Atlantic-origin water from Fram Strait to Denmark Strait, but substantial mixing with the interior basins occurs along its path (Fig. 12, Strass et al., 1993; Rudels et al., 2002; Jeansson et al., 2008; Håvik et al., 2019). The mixing takes place primarily in the Greenland Sea between 75 and 76°N and in the Iceland Sea between 68.5 and 69.5°N, where the East Greenland Current bifurcates into the separated and shelf break branches (Våge et al., 2013; Håvik et al., 2019). At Hornbanki, 300 km upstream of Denmark Strait, only 20 ± 1% of the separated and shelf break East Greenland Current branches stem from the Atlantic Domain, while the Greenland and Iceland Seas account for 50 ± 2% and 26 ± 6%, respectively. In agreement with Håvik et al. (2017), we also find an outer core of the East Greenland Current north of the West Jan Mayen Ridge. This outer core provides an important pathway for dense water formed in the central Greenland Sea towards Denmark Strait. The overflow water supplied by the NIJ originates primarily in the Greenland Sea (82 ± 2%), corroborating the results of Huang et al. (2020). This water follows two distinct pathways from the Greenland Sea to the slope north of Iceland: the outer core of the East Greenland Current and another, previously unknown, pathway across the Jan Mayen Ridge into the Iceland Sea. Within the Iceland Sea the water follows the cyclonic gyre, which leads to a southward flow along Kolbeinsey Ridge to the slope north of Iceland.

Although the upstream sources of the DSOW are in broad agreement with previous studies, we find a substantially lower contribution from

the Arctic Ocean than indicated by Tanhua et al. (2005) and Jeansson et al. (2008), who also included both hydrographic and geochemical observations. In addition to uncertainty in their contributions related to the spatial variability of water masses, the discrepancy is likely a result of temporal variability. Neither Tanhua et al. (2005) and Jeansson et al. (2008) nor the TMI solution properly account for temporal variability in water-mass properties. Substantial short-term variability is observed in both volume transport and hydrographic properties of the DSOW (e.g., Jochumsen et al., 2017; Mastropole et al., 2017; Lin et al., 2020) and the production and hydrographic properties of the source water masses vary inter-annually (Våge et al., 2015; Lauvset et al., 2018; Jeansson et al., 2017; Brakstad et al., 2019; Mork et al., 2019). Both Tanhua et al. (2005) and Jeansson et al. (2008) performed sensitivity simulations, where the end-member properties were allowed to vary within the variance of each parameter, to validate the effect of temporal variability in their source water compositions. This indicated relative mean errors of 30%–40%, and higher for some of the Arctic Ocean end-members (Jeansson et al., 2008). Similar sensitivity simulations with the TMI inversion would be computationally demanding, which is the reason our uncertainty estimates represent only the uncertainty related to the first guess of the pathway matrix and not temporal variability (Section 3.2). It is important to note that uncertainties related to temporal variability in hydrographic and geochemical properties were included as constraints in the inversion when optimizing the 2000–2019 winter-mean solution.

The two main contributors to the FBCOW is dense water formed in the Greenland Sea (46 ± 8%) and the Arctic Ocean (25 ± 9%). These source regions also supply the densest part of the overflow, while the less dense components stem from the Iceland Sea (10 ± 1%), the Atlantic Domain (11 ± 1%), and the North Atlantic (9 ± 0%). Dense water formed in the Greenland Sea and Arctic Ocean flows southward from the Greenland Sea along two distinct pathways. One corresponds to the recently documented IFSJ (Semper et al., 2020) and one follows the eastern side of the Jan Mayen Ridge (in accordance with e.g., Olsson et al., 2005; Voet et al., 2010; Serra et al., 2010; Huang et al., 2020; Hátún et al., 2021). Half (48 ± 3%) of the FBCOW transported with the IFSJ originates in the Greenland Sea, while 11 ± 6% stems from the Arctic Ocean. The majority of these dense waters flow across the sloping Jan Mayen Ridge and cyclonically around the Iceland Sea, similar to the dense water that supplies the NIJ. Some mixing occurs along the IFSJ path, which results in a 16 ± 3% contribution from the Iceland Sea, 18 ± 1% from the Atlantic Domain, and 7 ± 1% from the North Atlantic. The pathway along the Jan Mayen Ridge turns east and crosses over to the Norwegian continental slope, where it follows the eastern margin southwards to the Faroe-Shetland Channel. In agreement with Chafik et al. (2020), we find that this pathway is situated deep (>1000 m) in the water column and supplies the densest component of the FBCOW. In total, this pathway accounts for 24 ± 3% of the FBCOW, while the IFSJ supplies 58 ± 3%. The remaining portion is AW that is densified in the Faroe Current and recirculates around the Faroe Islands (18 ± 1%).

The fractional contributions from the Greenland Sea and Arctic Ocean to the overflow water transported by the IFSJ may be underestimated due to the light density bias in the IFSJ core. Semper et al. (2020) used one survey of high-resolution (2.5–10 km) hydrographic transects following the IFSJ to document its structure and properties. Based on 30 years of repeat hydrographic transects north of the Faroe Islands, they found that only 38 of the 120 surveys captured the upsloping dense water associated with the current due to the lower horizontal resolution (20 km). Hence, the densest water in the IFSJ is not well captured north of the Faroe Islands in the observations, which in turn impacts the TMI solution. Nevertheless, the TMI solution can help identify key locations where high-resolution observations are needed to properly resolve the currents feeding the overflows, such as north of the Faroe Islands and along the Jan Mayen Ridge.

The overflow water pathways resolved by the inversion represent the steady-state circulation that best fits the late-winter hydrographic and geochemical properties in the Nordic Seas between 2000 and 2019. Although water-mass properties vary within this period, it is considered sufficiently stable in terms of dense-water formation and water column structure (i.e., Brakstad et al., 2019; Somavilla, 2019). Considering the last 50 years, substantial changes have been observed in water-mass production and properties in the Nordic Seas (e.g., Eldevik et al., 2009; Våge et al., 2015; Lauvset et al., 2018; Brakstad et al., 2019; Smedsrud et al., 2022; Våge et al., 2022). Multiple inversions covering different decades or the inclusion of an age tracer similar to Schlitzer (2007) or Gebbie and Huybers (2012) are needed to determine how the time-evolving source regions and flow structure have influenced the overflows. The inclusion of an age tracer would also make it possible to estimate the residence times and the rate of exchange between water masses, which could be used to diagnose the propagation of heat or anthropogenic carbon into the deep ocean as demonstrated by Davila et al. (2022) with a global version of the TMI method. As opposed to numerical simulations, the TMI method observationally constrains and quantifies the net effect of advection and diffusion on the distribution of water masses (Gebbie and Huybers, 2010). Our results provide a step toward understanding how the dense overflow waters are supplied at present. This is crucial to better understand the impact of climate-driven changes, such as global warming and sea-ice retreat, which are projected to reduce dense-water formation in the interior of the Nordic Seas in the future (Moore et al., 2015, 2022; Bretones et al., 2022).

Declaration of competing interest

The authors declare that they have no known competing financial interests or personal relationships that could have appeared to influence the work reported in this paper.

Data availability

Access to the individual hydrographic and geochemical data sources are listed in Table 1. The combined and quality-controlled data set, covering the period 1950–2019, is available at the Norwegian Marine Data Centre (NMDC; https://doi.org/10.21335/NMDC-1271328906). The late-winter (February to April) climatology for the period 2000–2019 is available at https://doi.org/10.21335/NMDC-1518531676. Sea-ice concentrations were obtained from Walsh et al. (2015), while surface geostrophic velocities from satellite were obtained from the Copernicus Marine Environment Monitoring Service (http://marine.copernicus.eu).

Acknowledgments

Appendix A. Observational quality control

All hydrographic profiles were required to include both temperature and salinity measurements within the range −2–30 °C and 0–36 g kg^{-1}, respectively. Profiles with density inversions exceeding 0.05 kg m^{-3} were excluded unless the inversion was associated with a single data spike, in which case the spike was removed. We also required positive concentrations for the geochemical parameters and that all profiles had a minimum length of 3 data points. The same data are often stored in multiple archives. In many cases, however, the profiles are not exact duplicates. They can be interpolated to different vertical resolutions, truncated to different depths, or be ship-board CTD measurements and

bottle data recorded at the same cast (e.g., Behrendt et al., 2018). The position, time, and data can also vary slightly if they are rounded to different decimals. To detect these duplicates we compared each profile (position, time, and hydrography) to all other profiles within 1° longitude/latitude and ±5 days. Each profile pair that was compared was truncated to the depth range shared by both profiles and interpolated to the same vertical resolution. Profiles were considered duplicates if they were acquired less than 0.5 days and 1 km apart or if the temperature and salinity profiles matched to the second and third decimal, respectively. Several of the duplicates were visually inspected. This was necessary to detect, for example, truncated duplicates (or bottle data) that had been linearly interpolated to higher resolution. In general, we kept the profile with most information and excluded truncated and hydrographic bottle data. If a profile pair had similar resolution we retained the profile from the most original source. We also prioritized data from UDASH (Behrendt et al., 2018), which have already gone through a thorough quality control.

After erroneous and duplicate data were removed, we divided the dataset into three different periods (1950–1979, 1980–1999, and 2000–2019) that were inspected for outliers separately. Each hydrographic profile was compared to all other profiles from the same period within a radius of 110 km (approximately 1° of latitude, Våge et al., 2013). In the Nordic Seas water-mass properties tend to vary more across than along topographic gradients because of the close alignment between currents and bathymetry (Nøst and Isachsen, 2003). This was accounted for by adjusting the distance to the other profiles (r) according to Davis (1998), Skagseth and Mork (2012), and Våge et al. (2013) as:

$$r^2 = |x_g - x_o|^2 + \left|3\lambda \frac{H_g - H_o}{H_g + H_o}\right|^2, \tag{A.1}$$

where $x_g(x_o)$ is the geographical position of the profile in question (all other profiles) and $H_g(H_o)$ is the corresponding depth based on ETOPO1 (Amante and Eakins, 2009). The topographic parameter $\lambda =$ 100 km (Lavender et al., 2005; Voet et al., 2010; Skagseth and Mork, 2012; Våge et al., 2013). The difference in bottom depth determines the magnitude of the adjustment, and the result is an effective radius that is increased along isobaths. All profiles within an effective radius of 110 km were then interpolated onto a common vertical coordinate with 5-m resolution. Profiles that differed from the mean, at any depth, by more than six standard deviations were considered outliers and removed.

A slightly different procedure was used for the geochemical data due to the generally lower vertical and horizontal resolution. All geochemical profiles were interpolated onto 46 depth levels with intervals ranging from 10 m near the surface to 250 m at depth (same as the TMI resolution, Fig. C.1f), before the mean and standard deviation in each time period were calculated. Profiles were then identified as outliers and removed if they differed from the mean by more than six standard deviations.

Appendix B. Mixed-layer depths

For the Iceland and Greenland Seas we used late-winter (February–April) mixed-layer depths from Våge et al. (2015) and Brakstad et al. (2019), respectively. These were determined by a procedure involving two independent automated routines: one based on a density-difference criterion (Nilsen and Falck, 2006) and one based on the curvature of the temperature profile (Lorbacher et al., 2006). If neither of the automated routines accurately identified the base of the mixed layer, which was verified by visual inspection of each hydrographic profile, it was determined by a manual procedure developed by Pickart et al. (2002). This manual procedure was used for 44% (Våge et al., 2015) and 39% (Brakstad et al., 2019) of the profiles in the Iceland and Greenland Seas, respectively. The automated routines performed well for profiles having a pronounced density gradient below the base of the mixed layer, but this is often not the case during winter in the Iceland

and Greenland Seas where the entire water column is weakly stratified. The same semi-automatic procedure was employed here to update the Iceland and Greenland Seas mixed-layer databases such that the entire 2000–2019 period was covered.

For the rest of the domain, where the density stratification is stronger, late-winter mixed-layer depths were estimated based on the density-difference criterion (Nilsen and Falck, 2006). That is, the base of the mixed layer was identified as the depth where the increase in potential density from the surface reached $\Delta\rho = \rho(T_0 - \Delta T, S_0) - \rho(T_0, S_0)$. The density difference $\Delta\rho$ varies with measured surface temperature (T_0) and salinity (S_0), which provides more accurate results than using a constant value (de Boyer Montégut et al., 2004; Nilsen and Falck, 2006). As de Boyer Montégut et al. (2004), Våge et al. (2015), and Brakstad et al. (2019) we used $\Delta T = 0.2\ °C$.

The late-winter mixed-layer properties were interpolated onto a regular 1/3° longitude by 1/8° latitude grid as described in Appendix C (Eq. (C.1)). Only the 75% deepest mixed layers were included in each grid cell to remove re-stratified profiles and profiles taken prior to the onset of convection. Changing this limit by ±10% had an impact almost exclusively on the Greenland Sea gyre and the average difference within the gyre was ±50 m, which is small compared to the total mean mixed-layer depth (555 m, within the white contour in Fig. B.1). For polar, ice-covered regions where winter data are scarce, we used the available data to estimate mean mixed-layer properties. These were then applied to the entire sea-ice-covered area (north of the annual-mean 50% sea-ice concentration contour marked in blue in Fig. B.1). The sea-ice concentration data were obtained from the National Snow and Ice Data Center (Walsh et al., 2015, 2017). The final gridded mixed-layer product shown in Fig. B.1 was smoothed by convolution with a Gaussian window of size 9 × (1/3° longitude and 1/8° latitude).

Appendix C. Gridding and uncertainty estimates

All 2000–2019 observations of temperature, salinity, oxygen, nitrate, and phosphate were modified to represent late-winter conditions (Section 2.2) and used to construct the three-dimensional fields included in the TMI inversion. The value in each grid cell was computed from all measurements within an effective radius of 50 km. As in Appendix A (Eq. (A.1)), the effective radius was increased along isobaths to account for the greater correlation length scales along topography. The effective radius and the topographic parameter λ were modified to 120 km and 300 km, respectively, in the sea-ice covered area (north of the annual mean 50% sea-ice concentration contour, Fig. B.1). This was done to improve the representation of the East Greenland Current in the inversion, which was generally not well constrained due to the sparse data coverage in this region (Fig. 2). The result of both increased radius and λ was that more observations were included in each grid cell, but only from along the bathymetry.

The average value $\bar{x}_i$ in each grid cell i was weighted by the inverse distance as:

$$\bar{x}_i = \frac{\sum_{t=1}^{N_i} \omega_{it} x_{it}}{\sum_{t=1}^{N_i} \omega_{it}} = \sum_{t=1}^{N_i} \omega'_{it} x_{it}, \tag{C.1}$$

where x_{it} is measurement number t and N_i is the total number of observations contributing to the weighted average. ω_{it} is the inverse distance to each observation and $\omega'_{it} = \omega_{it} / \sum_{t=1}^{N_i} \omega_{it}$.

The uncertainty of the final gridded product representing the climatological winter conditions between 2000 and 2019 depends on the amount of observations included in the estimate and their variance. In general, the uncertainty decreases with depth due to the lower variance at depth and with increased number of observations. For each grid cell we estimated the variance $\hat{\sigma}_i^2$ as:

$$\hat{\sigma}_i^2 = \frac{1}{N-m} \sum_{i=1}^{m} \sum_{t=1}^{N_i} (x_{it} - \bar{x}_i)^2, \tag{C.2}$$
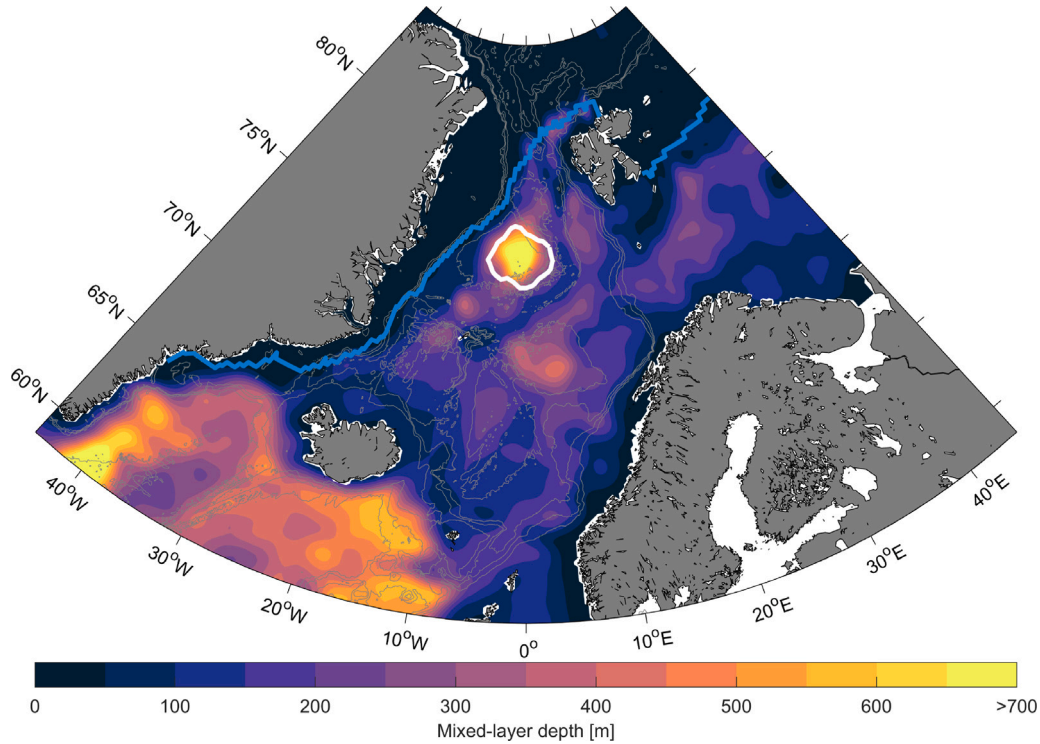
Fig. B.1. Late-winter (February–April) mixed-layer depth between 2000 and 2019. The blue line marks the annual-mean (2000–2013) 50% sea-ice concentration contour from Walsh et al. (2015), while the white contour outlines the Greenland Sea gyre (Moore et al., 2015). The 500-, 1000-, 1500-, and 3000-m isobaths are shown as thin gray contours.

where N is the total number of observations and m is the total number of ocean grid cells at the corresponding depth level. That is, all observations across the entire domain at each depth level were used to estimate the expected variance for each grid cell at the same level. The uncertainty ε_i was then defined as:

$$\varepsilon_i = \hat{\sigma}_i \sqrt{\sum_{t=1}^{N_i} (\omega'_{it})^2}, \tag{C.3}$$

which decreases with number of observations (weighted according to distance to the grid cell in question). The resulting uncertainty profiles (overall means and standard deviations) are shown in Fig. C.1.

Appendix D. First guess of the pathway matrix *A*

The first guess of the mass fractions *m* that form the pathway matrix *A* was constructed based on gradients in potential density and the geostrophic stream function. To obtain absolute geostrophic velocities we used surface geostrophic velocity from satellite altimeter data as reference (Section 3.2, Fig. D.1). The surface geostrophic velocity is very patchy in sea-ice covered areas due to large uncertainty. The hydrographic data coverage is also very sparse in the same region (Fig. 2). As a consequence, we decided to keep the isotropic first guess (Gebbie and Huybers, 2010; Gebbie, 2014) in areas with annual-mean sea-ice concentration exceeding 80% (north of the blue line in Fig. D.1). In the open ocean we assumed that large gradients in potential density and the geostrophic stream function lead to weak exchange between neighboring grid cells (i.e. small mass fractions).

Half of the mass fractions were determined by gradients in potential density (σ_Θ), while the remaining half was determined by gradients in the geostrophic stream function (ψ). For each interior grid cell i, the sum of the mass fractions m_{ij} from the neighboring grid cells j can be expressed as:

$$\sum_{j=1}^{N} m_{ij} = \frac{1}{2} \sum_{j=1}^{N} m_{ij}^{\Delta\sigma_\Theta} + \frac{1}{2} \sum_{j=1}^{N} m_{ij}^{\Delta\psi} = 1, \tag{D.1}$$

where $m_{ij}^{\Delta\sigma_\Theta}$ and $m_{ij}^{\Delta\psi}$ are the mass fractions determined by gradients in σ_Θ and ψ, respectively. Below the mixed layer, $m_{ij}^{\Delta\sigma_\Theta}$ was calculated based on gradients in σ_Θ as:

$$m_{ij}^{\Delta\sigma_\Theta} = \frac{|\Delta\sigma_{\Theta ij,max}| - |\Delta\sigma_{\Theta ij}| + 10^{-4}}{\sum_{j=1}^{N}(|\Delta\sigma_{\Theta ij,max}| - |\Delta\sigma_{\Theta ij}| + 10^{-4})}, \tag{D.2}$$

where $\Delta\sigma_{\Theta ij}$ is the density difference between the grid cell in question (i) and its neighbor j. $\Delta\sigma_{\Theta ij,max}$ is the density difference to the neighbor with the largest difference. That is, a larger gradient leads to a smaller mass fraction and weaker exchange. The constant 10^{-4} is added for regularization. Vertical mixing dominates within the mixed layer, where the density is homogeneous. Hence, we prescribed $m_{ij}^{\Delta\sigma_\Theta}$ to represent exchange with the neighbor located vertically above the grid cell in question.

The mass fractions $m_{ij}^{\Delta\psi}$ based on the geostrophic stream function only include horizontal contributions in the direction of the geostrophic flow. That is, if the geostrophic flow was from the north-east, the only non-zero mass fractions $m_{ij}^{\Delta\psi}$ would be the mass fractions from the northern and eastern neighbors. The magnitude of the non-zero mass fractions was calculated as:

$$m_{ij}^{\Delta\psi_{x(y)}} = \frac{|\Delta\psi_{x(y)}|}{\sum_{j=1}^{N}(|\Delta\psi_{xy}|)}, \tag{D.3}$$

where $\Delta\psi_x$ and $\Delta\psi_y$ are the longitudinal and latitudinal differences in the geostrophic stream function, respectively. This means that if $\Delta\psi_x >$ 0 (southward geostrophic flow component), the neighbor to the north
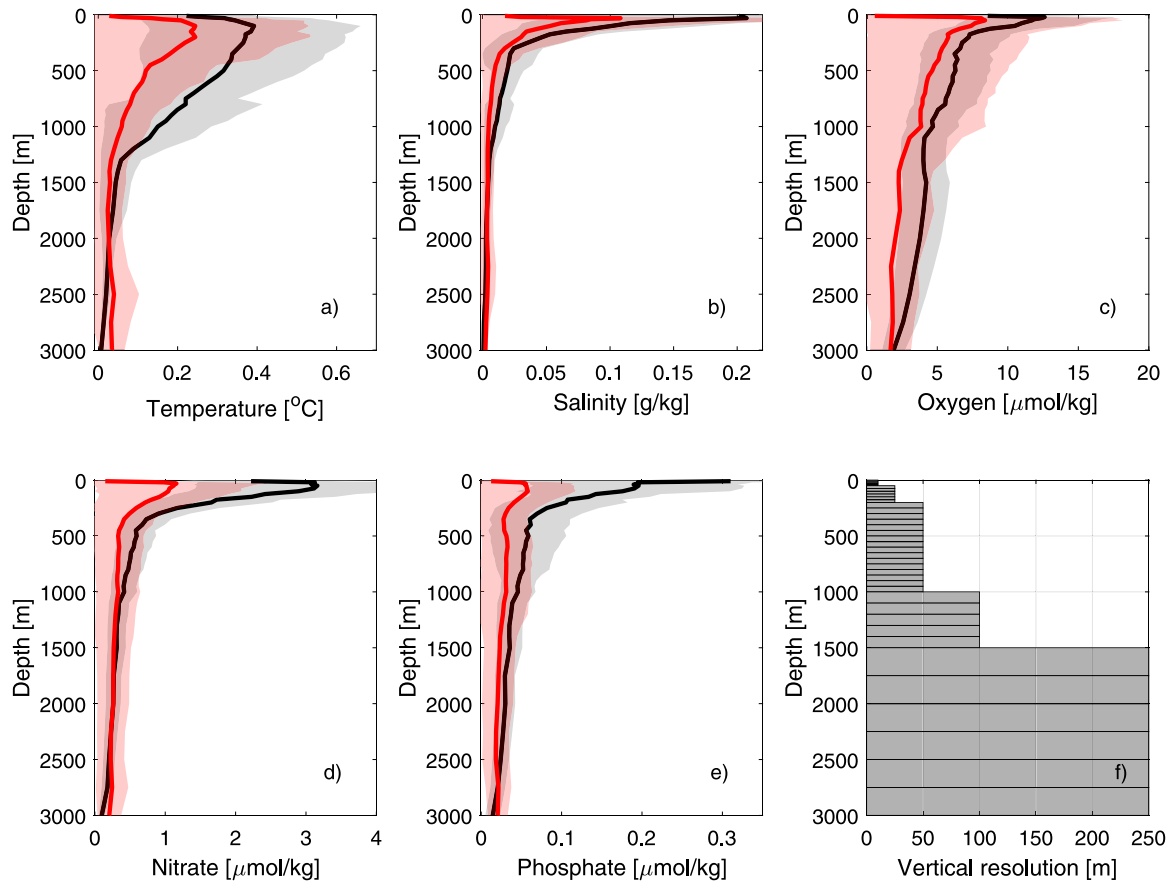
Fig. C.1. Mean observational uncertainty (black) and mean misfit (red) between the TMI and observed temperature (a), salinity (b), oxygen (c), nitrate (d), and phosphate (e) in the upper 3000 m of the water column. The shading indicates ±1 standard deviation. The TMI vertical resolution is shown by the gray bars in f).
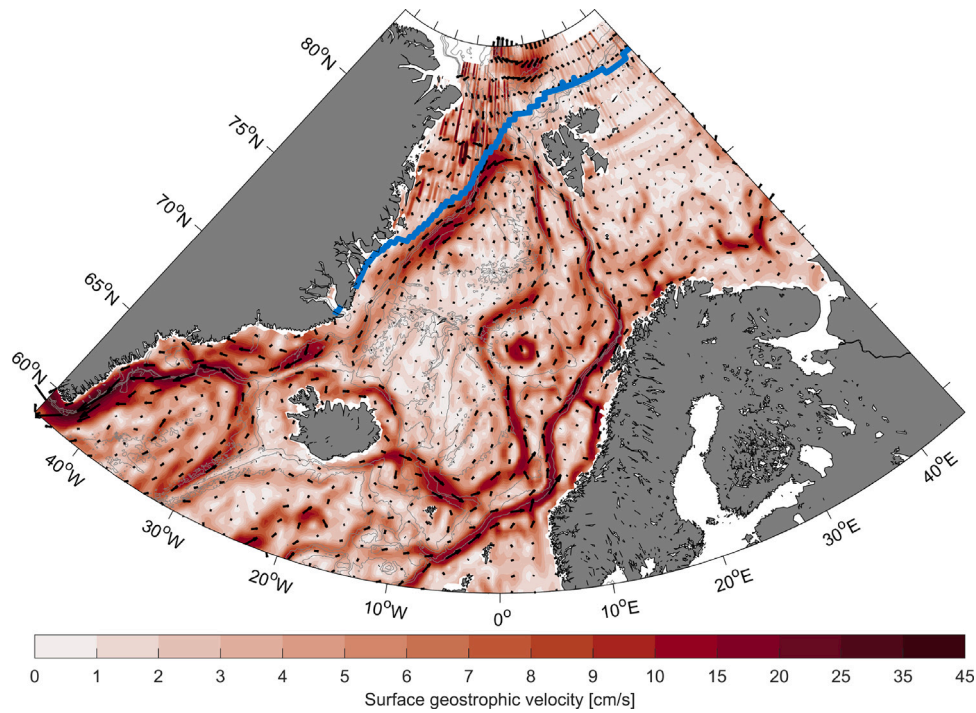

Fig. D.1. Annual-mean surface geostrophic velocity between 2000 and 2019 from the gridded satellite altimeter product. The blue line indicates the mean (2000–2013) 80% sea-ice concentration contour from Walsh et al. (2015). The 500-, 1000-, 1500-, and 3000-m isobaths are shown as thin gray contours.

contributes with a non-zero mass fraction with the magnitude $m_{ij}^{\Delta\psi_x}$. The first guess of the pathway matrix $\boldsymbol{A}$ based on $m_{ij}^{\Delta\sigma_\Theta}$ and $m_{ij}^{\Delta\psi}$ resulted in more advective pathways and a better (less diffuse) representation of the ocean state. The running time of the inversion was also significantly reduced.

References

Aagaard, K., Swift, J.H., Carmack, E.C., 1985. Thermohaline circulation in the Arctic Mediterranean Seas. J. Geophys. Res. 90 (NC3), 4833–4846. http://dx.doi.org/10.1029/JC090iC03p04833.

Amante, C., Eakins, B.W., 2009. ETOPO1 1 Arc-Minute Global Relief Model: Procedures, Data Sources, and Analysis. Technical Report, National Geophysical Data Center, NOAA, http://dx.doi.org/10.7289/V5C8276M, NOAA Technical Memorandum NESDIS NGDC-24.

Anderson, L.A., Sarmiento, J.L., 1994. Redfield ratios of remineralization determined by nutrient data analysis. Glob. Biogeochem. Cycles 8 (1), 65–80. http://dx.doi.org/10.1029/93GB03318.

Behrendt, A., Sumata, H., Rabe, B., Schauer, U., 2018. UDASH–unified database for Arctic and Subarctic hydrography. Earth Syst. Sci. Data 10 (2), 1119–1138. http://dx.doi.org/10.5194/essd-10-1119-2018.

Berx, B., Hansen, B., Østerhus, S., Larsen, K.M., Sherwin, T., Jochumsen, K., 2013. Combining in situ measurements and altimetry to estimate volume, heat and salt transport variability through the Faroe–Shetland Channel. Ocean Sci. 9 (4), 639–654. http://dx.doi.org/10.5194/os-9-639-2013.

Brakstad, A., Våge, K., Håvik, L., Moore, G.W.K., 2019. Water mass transformation in the Greenland Sea during the period 1986–2016. J. Phys. Oceanogr. 49 (1), 121–140. http://dx.doi.org/10.1175/JPO-D-17-0273.1.

Bretones, A., Nisancioglu, K.H., Jensen, M.F., Brakstad, A., Yang, S., 2022. Transient increase in Arctic deep-water formation and ocean circulation under sea ice retreat. J. Clim. 35 (1), 109–124. http://dx.doi.org/10.1175/JCLI-D-21-0152.1.

Casanova-Masjoan, M., Pérez-Hernández, M.D., Pickart, R.S., Valdimarsson, H., Ólafsdóttir, S.R., Macrander, A., Grisolía-Santos, D., Torres, D.J., Jónsson, S., Våge, K., Lin, P., Hernández-Guerra, A., 2020. Along-stream, seasonal, and interannual variability of the North Icelandic Irminger Current and East Icelandic Current around Iceland. J. Geophys. Res.: Oceans 125 (9), e2020JC016283. http://dx.doi.org/10.1029/2020JC016283.

Chafik, L., Hátún, H., Kjellsson, J., Larsen, K.M.H., Rossby, T., Berx, B., 2020. Discovery of an unrecognized pathway carrying overflow waters toward the Faroe Bank Channel. Nature Commun. 11 (1), 1–10. http://dx.doi.org/10.1038/s41467-020-17426-8.

Chafik, L., Rossby, T., 2019. Volume, heat, and freshwater divergences in the subpolar North Atlantic suggest the Nordic Seas as key to the state of the meridional overturning circulation. Geophys. Res. Lett. 46, 4799–4808. http://dx.doi.org/10.1029/2019GL082110.

Davila, X., Gebbie, G., Brakstad, A., Lauvset, S.K., McDonagh, E.L., Schwinger, J., Olsen, A., 2022. How is the ocean anthropogenic carbon reservoir filled? Glob. Biogeochem. Cycles 36 (5), e2021GB007055. http://dx.doi.org/10.1029/2021GB007055.

Davis, R.E., 1998. Preliminary results from directly measuring middepth circulation in the tropical and South Pacific. J. Geophys. Res. 103 (C11), 24619–24639. http://dx.doi.org/10.1029/98JC01913.

de Boyer Montégut, C., Madec, G., Fischer, A.S., Lazar, A., Iudicone, D., 2004. Mixed layer depth over the global ocean: an examination of profile data and a profile-based climatology. J. Geophys. Res.: Oceans 109 (C12), http://dx.doi.org/10.1029/2004JC002378.

de Jong, M.F., Søiland, H., Bower, A.S., Furey, H.H., 2018. The subsurface circulation of the Iceland sea observed with RAFOS floats. Deep-Sea Res. I 141, 1–10. http://dx.doi.org/10.1016/j.dsr.2018.07.008.

Dickson, R.R., Brown, J., 1994. The production of North Atlantic deep water: sources, rates, and pathways. J. Geophys. Res. 99 (C6), 12319–12341. http://dx.doi.org/10.1029/94jc00530.

Eldevik, T., Nilsen, J.E.Ø., Iovino, D., Olsson, K.A., Sandø, A.B., Drange, H., 2009. Observed sources and variability of Nordic Seas overflow. Nat. Geosci. 2 (6), 405–409. http://dx.doi.org/10.1038/ngeo518.

Fogelqvist, E., Blindheim, J., Tanhua, T., Østerhus, S., Buch, E., Rey, F., 2003. Greenland - Scotland overflow studied by hydro-chemical multivariate analysis. Deep-Sea Res. I 50 (1), 73–102. http://dx.doi.org/10.1016/s0967-0637(02)00131-0.

Frigstad, H., Andersen, T., Bellerby, R.G.J., Silyakova, A., Hessen, D.O., 2014. Variation in the seston C:N ratio of the Arctic Ocean and pan-Arctic shelves. J. Mar. Syst. 129, 214–223. http://dx.doi.org/10.1016/j.jmarsys.2013.06.004.

Garcia-Quintana, Y., Grivault, N., Hu, X., Myers, P.G., 2021. Dense water formation on the Icelandic shelf and its contribution to the North Icelandic Jet. J. Geophys. Res.: Oceans 126 (8), e2020JC016951. http://dx.doi.org/10.1029/2020JC016951.

Gebbie, G., 2014. How much did Glacial North Atlantic Water shoal? Paleoceanography 29 (3), 190–209. http://dx.doi.org/10.1002/2013PA002557.

Gebbie, G., Huybers, P., 2010. Total matrix intercomparison: a method for determining the geometry of water-mass pathways. J. Phys. Oceanogr. 40 (8), 1710–1728. http://dx.doi.org/10.1175/2010JPO4272.1.

Gebbie, G., Huybers, P., 2011. How is the ocean filled? Geophys. Res. Lett. 38 (6), http://dx.doi.org/10.1029/2011GL046769.

Gebbie, G., Huybers, P., 2012. The mean age of ocean waters inferred from radiocarbon observations: sensitivity to surface sources and accounting for mixing histories. J. Phys. Oceanogr. 42 (2), 291–305. http://dx.doi.org/10.1175/JPO-D-11-043.1.

Gilbert, J.C., Lemaréchal, C., 1989. Some numerical experiments with variable-storage quasi-Newton algorithms. Math. Program. 45 (1), 407–435. http://dx.doi.org/10.1007/BF01589113.

Glover, D.M., Jenkins, W.J., Doney, S.C., 2011. Modeling Methods for Marine Science. Cambridge University Press.

Hansen, B., Østerhus, S., 2000. North Atlantic-Nordic Seas exchanges. Prog. Oceanogr. 45 (2), 109–208. http://dx.doi.org/10.1016/s0079-6611(99)00052-x.

Harden, B.E., Pickart, R.S., Valdimarsson, H., Våge, K., de Steur, L., Richards, C., Bahr, F., Torres, D., Børve, E., Jónsson, S., Macrander, A., Østerhus, S., Håvik, L., Hattermann, T., 2016. Upstream sources of the Denmark strait overflow: observations from a high-resolution mooring array. Deep-Sea Res. I 112, 94–112. http://dx.doi.org/10.1016/j.dsr.2016.02.007.

Hátún, H., Chafik, L., Larsen, K.M.H., 2021. The Norwegian Sea Gyre – a regulator of Iceland–Scotland Ridge exchanges. Front. Mar. Sci. 8 (694614), http://dx.doi.org/10.3389/fmars.2021.694614.

Håvik, L., Almansi, M., Våge, K., Haine, T.W.N., 2019. Atlantic-origin overflow water in the East Greenland Current. J. Phys. Oceanogr. 49 (9), 2255–2269. http://dx.doi.org/10.1175/JPO-D-18-0216.1.

Håvik, L., Pickart, R.S., Våge, K., Torres, D., Thurnherr, A.M., Beszczynska-Möller, A., Walczowski, W., von Appen, W.-J., 2017. Evolution of the East Greenland Current from Fram Strait to Denmark strait: synoptic measurements from summer 2012. J. Geophys. Res.: Oceans 122 (3), 1974–1994. http://dx.doi.org/10.1002/2016JC012228.

Helland-Hansen, B., Nansen, F., 1909. The Norwegian Sea: its physical oceanography based upon the Norwegian researches 1900–1904. Rep. Nor. Fish. Mar. Investig. 2 (2), 1–390.

Huang, J., Pickart, R.S., Huang, R.X., Lin, P., Brakstad, A., Xu, F., 2020. Sources and upstream pathways of the densest overflow water in the Nordic Seas. Nature Commun. 11 (5389), http://dx.doi.org/10.1038/s41467-020-19050-y.

IOC, SCOR, IAPSO, 2010. The international thermodynamic equation of seawater - 2010: calculation and use of thermodynamic properties. In: Intergovernmental Oceanographic Commission, Manuals and Guides No. 56. UNESCO.

Isachsen, P.E., Mauritzen, C., Svendsen, H., 2007. Dense water formation in the Nordic Seas diagnosed from sea surface buoyancy fluxes. Deep-Sea Res. I 54 (1), 22–41. http://dx.doi.org/10.1016/j.dsr.2006.09.008.

Jeansson, E., Bellerby, R.G.J., Skjelvan, I., Frigstad, H., Ólafsdóttir, S.R., Olafsson, J., 2015. Fluxes of carbon and nutrients to the Iceland Sea surface layer and inferred primary productivity and stoichiometry. Biogeosciences 12 (3), 875–885. http://dx.doi.org/10.5194/bg-12-875-2015.

Jeansson, E., Jutterström, S., Rudels, B., Anderson, L.G., Olsson, K.A., Jones, E.P., Smethie, W.M., Swift, J.H., 2008. Sources to the East Greenland Current and its contribution to the Denmark strait overflow. Prog. Oceanogr. 78 (1), 12–28. http://dx.doi.org/10.1016/j.pocean.2007.08.031.

Jeansson, E., Olsen, A., Jutterström, S., 2017. Arctic intermediate water in the Nordic Seas, 1991–2009. Deep-Sea Res. I 128, 82–97. http://dx.doi.org/10.1016/j.dsr.2017.08.013.

Jochumsen, K., Moritz, M., Nunes, N., Quadfasel, D., Larsen, K.M., Hansen, B., Valdimarsson, H., Jónsson, S., 2017. Revised transport estimates of the Denmark strait overflow. J. Geophys. Res. 122, 3434–3450. http://dx.doi.org/10.1002/2017JC012803.

Jónsson, S., Valdimarsson, H., 2012. Water mass transport variability to the north Icelandic shelf, 1994—2010. ICES J. Mar. Sci. 69 (5), 809–815. http://dx.doi.org/10.1093/icesjms/fss024.

Karstensen, J., Schlosser, P., Wallace, D.W.R., Bullister, J.L., Blindheim, J., 2005. Water mass transformation in the Greenland Sea during the 1990s. J. Geophys. Res. 110 (C7), http://dx.doi.org/10.1029/2004jc002510.

Köhl, A., 2010. Variable source regions of Denmark Strait and Faroe Bank Channel overflow waters. Tellus A 62 (4), 551–568. http://dx.doi.org/10.1111/j.1600-0870.2010.00454.x.

Köhl, A., Willebrand, J., 2002. An adjoint method for the assimilation of statistical characteristics into eddy-resolving ocean models. Tellus A 54 (4), 406–425. http://dx.doi.org/10.3402/tellusa.v54i4.12150.

Langehaug, H.R., Brakstad, A., Våge, K., Jeansson, E., Ilicak, M., Katsman, C.A., 2022. Drivers of surface salinity changes in the Greenland–Iceland Seas on seasonal and interannual time scales - a climate model study. Earth Space Sci. Open Arch. http://dx.doi.org/10.1002/essoar.10511221.1.

Langehaug, H.R., Falck, E., 2012. Changes in the properties and distribution of the intermediate and deep waters in the Fram Strait. Prog. Oceanogr. 96 (1), 57–76. http://dx.doi.org/10.1016/j.pocean.2011.10.002.

Latarius, K., Quadfasel, D., 2010. Seasonal to inter-annual variability of temperature and salinity in the Greenland Sea Gyre: heat and freshwater budgets. Tellus A 62 (4), 497–515. http://dx.doi.org/10.1111/j.1600-0870.2010.00453.x.

Lauvset, S.K., Brakstad, A., Våge, K., Olsen, A., Jeansson, E., Mork, K.A., 2018. Continued warming, salinification and oxygenation of the Greenland Sea gyre. Tellus A 70 (1), 1–9. http://dx.doi.org/10.1080/16000870.2018.1476434.

Lavender, K.L., Owens, W.B., Davis, R.E., 2005. The mid-depth circulation of the subpolar North Atlantic Ocean as measured by subsurface floats. Deep-Sea Res. I 52 (5), 767–785. http://dx.doi.org/10.1016/j.dsr.2004.12.007.

Lin, P., Pickart, R.S., Jochumsen, K., Moore, G.W.K., Valdimarsson, H., Fristedt, T., Pratt, L.J., 2020. Kinematic structure and dynamics of the Denmark Strait overflow from ship-based observations. J. Phys. Oceanogr. 50 (11), 3235–3251. http://dx.doi.org/10.1175/JPO-D-20-0095.1.

Lorbacher, K., Dommenget, D., Niiler, P.P., Köhl, A., 2006. Ocean mixed layer depth: A subsurface proxy of ocean - atmosphere variability. J. Geophys. Res. 111 (C7), http://dx.doi.org/10.1029/2003JC002157.

Lozier, S.M., Li, F., Bacon, S., Bahr, F., Bower, A.S., Cunningham, S.A., de Jong, F.M., de Steur, L., deYoung, B., Fischer, J., Gary, S.F., Greenan, B.J.W., Holliday, N.P., Houk, A., Houpert, L., Inall, M.E., Johns, W.E., Johnson, H.L., Johnson, C., Karstensen, J., Koman, G., Le Bras, I.A., Lin, X., Mackay, N., Marshall, D.P., Mercier, H., Oltmanns, M., Pickart, R.S., Ramsey, A.L., Rayner, D., Straneo, F., Thierry, V., Torres, D.J., Williams, R.G., Wilson, C., Yang, J., Yashayaev, I., Zhao, J., 2019. A sea change in our view of overturning in the subpolar North Atlantic. Science 363, 516–521. http://dx.doi.org/10.1126/science.aau6592.

Malmberg, S.A., 1983. Hydrographic Investigations in the Iceland and Greenland Seas in Late Winter 1971 - "Deep Water Project", Vol. 33. Jökull.

Marshall, J., Schott, F., 1999. Open - ocean convection: observations, theory, and models. Rev. Geophys. 37 (1), 1–64. http://dx.doi.org/10.1029/98RG02739.

Mastropole, D., Pickart, R.S., Valdimarsson, H., Våge, K., Jochumsen, K., Girton, J., 2017. On the hydrography of Denmark strait. J. Geophys. Res. 122 (1), 306–321. http://dx.doi.org/10.1002/2016JC012007.

Mauritzen, C., 1996. Production of dense overflow waters feeding the North Atlantic across the Greenland–Scotland Ridge. Part 1: Evidence for a revised circulation scheme. Deep-Sea Res. I 43 (6), 769–806. http://dx.doi.org/10.1016/0967-0637(96)00037-4.

McKenna, C., Berx, B., Austin, W.E.N., 2016. The decomposition of the Faroe–Shetland Channel water masses using parametric optimum multi-parameter analysis. Deep-Sea Res. I 107, 9–21. http://dx.doi.org/10.1016/j.dsr.2015.10.013.

Meincke, J., Jónsson, S., Swift, J.H., 1992. Variability of convective conditions in the Greenland Sea. ICES Mar. Sci. Symp. 195, 32–39.

Meincke, J., Rudels, B., 1996. Greenland Sea Deep Water: A Balance Between Convection and Advection. World Meteorological Organization, pp. 436–440.

Messias, M.J., Watson, A.J., Johannessen, T., Oliver, K.I.C., Olsson, K.A., Fogelqvist, E., Olafsson, J., Bacon, S., Balle, J., Bergman, N., Budéus, G., Danielsen, M., Gascard, J.C., Jeansson, E., Olafsdottir, S.R., Simonsen, K., Tanhua, T., Van Scoy, K., Ledwell, J.R., 2008. The Greenland Sea tracer experiment 1996–2002: Horizontal mixing and transport of Greenland Sea Intermediate Water. Prog. Oceanogr. 78 (1), 85–105. http://dx.doi.org/10.1016/j.pocean.2007.06.005.

Moore, G.W.K., Våge, K., Pickart, R.S., Renfrew, I.A., 2015. Decreasing intensity of open-ocean convection in the Greenland and Iceland seas. Nature Clim. Change 5 (9), 877–882. http://dx.doi.org/10.1038/nclimate2688.

Moore, G.W.K., Våge, K., Renfrew, I.A., Pickart, R.S., 2022. Sea-ice retreat suggests reorganization of water mass transformation in the Nordic and Barents Seas. Nature Commun. 13 (1), 1–8. http://dx.doi.org/10.1038/s41467-021-27641-6.

Mork, K.A., Drinkwater, K.F., Jónsson, S., Valdimarsson, H., Ostrowski, M., 2014a. Water mass exchanges between the Norwegian and Iceland seas over the Jan Mayen Ridge using in-situ current measurements. J. Mar. Syst. 139, 227–240. http://dx.doi.org/10.1016/j.jmarsys.2014.06.008.

Mork, K.A., Skagseth, Ø., Ivshin, V., Ozhigin, V., Hughes, S.L., Valdimarsson, H., 2014b. Advective and atmospheric forced changes in heat and fresh water content in the Norwegian Sea, 1951–2010. Geophys. Res. Lett. 41 (17), 6221–6228. http://dx.doi.org/10.1002/2014GL061038.

Mork, K.A., Skagseth, Ø., Søiland, H., 2019. Recent warming and freshening of the Norwegian Sea observed by Argo data. J. Clim. 32 (12), 3695–3705. http://dx.doi.org/10.1175/JCLI-D-18-0591.1.

Nilsen, J.E.Ø., Falck, E., 2006. Variations of mixed layer properties in the Norwegian Sea for the period 1948–1999. Prog. Oceanogr. 70 (1), 58–90. http://dx.doi.org/10.1016/j.pocean.2006.03.014.

Nilsen, J.E.Ø., Hátún, H., Mork, K.A., Valdimarsson, H., 2008. The NISE Dataset, No. 08–01. Technical Report, Faroese Fisheries Laboratory, Box 3051, Tórshavn, Faroe Islands.

Nocedal, J., 1980. Updating quasi-Newton matrices with limited storage. Math. Comp. 35 (151), 773–782. http://dx.doi.org/10.1090/S0025-5718-1980-0572855-7.

Nøst, O.A., Isachsen, P.E., 2003. The large-scale time-mean ocean circulation in the Nordic Seas and Arctic Ocean estimated from simplified dynamics. J. Mar. Res. 61 (2), 175–210. http://dx.doi.org/10.1357/002224003322005069.

O'Dwyer, J., Kasajima, Y., Nøst, O.A., 2001. North Atlantic water in the Barents Sea opening, 1997 to 1999. Polar Res. 20 (2), 209–216. http://dx.doi.org/10.3402/polar.v20i2.6519.

Olsen, A., Key, R.M., van Heuven, S., Lauvset, S.K., Velo, A., Lin, X., Schirnick, C., Kozyr, A., Tanhua, T., Hoppema, M., Jutterström, S., Steinfeldt, R., Jeansson, E., Ishii, M., Pérez, F.F., Suzuki, T., 2016. The global ocean data analysis project version 2 (GLODAPv2) - an internally consistent data product for the world ocean. Earth Syst. Sci. Data 8, 297–323. http://dx.doi.org/10.5194/essd-8-297-2016.

Olsen, A., Lange, N., Key, R.M., Tanhua, T., Álvarez, M., Becker, S., Bittig, H.C., Carter, B.R., Cotrim da Cunha, L., Feely, R.A., van Heuven, S., Hoppema, M., Ishii, M., Jeansson, E., Jones, S.D., Jutterström, S., Karlsen, M.K., Kozyr, A., Lauvset, S.K., Lo Monaco, C., Murata, A., Pérez, F.F., Pfeil, B., Schirnick, C., Steinfeldt, R., Suzuki, T., Telszewski, M., Tilbrook, B., Velo, A., Wanninkhof, R., 2019. GLODAPv2.2019 - an update of GLODAPv2. Earth Syst. Sci. Data 11, 1437–1461. http://dx.doi.org/10.5194/essd-11-1437-2019.

Olsson, K.A., Jeansson, E., Anderson, L.G., Hansen, B., Eldevik, T., Kristiansen, R., Messias, M.-J., Johannessen, T., Watson, A.J., 2005. Intermediate water from the Greenland Sea in the Faroe Bank Channel: spreading of released sulphur hexafluoride. Deep-Sea Res. I 52 (2), 279–294. http://dx.doi.org/10.1016/j.dsr.2004.09.009.

Østerhus, S., Gammelsrød, T., 1999. The abyss of the Nordic Seas is warming. J. Clim. 12 (11), 3297–3304. http://dx.doi.org/10.1175/1520-0442(1999)012<3297:TAOTNS>2.0.CO;2.

Østerhus, S., Woodgate, R., Valdimarsson, H., Turrell, B., de Steur, L., Quadfasel, D., Olsen, S.M., Moritz, M., Lee, C.M., Larsen, K.M.H., Jonsson, S., Johnson, C., Jochumsen, K., Hansen, B., Curry, B., Cunningham, S., Berx, B., 2019. Arctic Mediterranean exchanges: a consistent volume budget and trends in transports from two decades of observations. Ocean Sci. 15 (2), 379–399. http://dx.doi.org/10.5194/os-15-379-2019.

Pickart, R.S., Torres, D.J., Clarke, R.A., 2002. Hydrography of the Labrador Sea during active convection. J. Phys. Oceanogr. 32 (2), 428–457. http://dx.doi.org/10.1175/1520-0485(2002)032<0428:hotlsd>2.0.co;2.

Redfield, A.C., Ketchum, B.H., Richards, F.A., 1963. The influence of organisms on the composition of seawater. In: Hill, M.N. (Ed.), In the Sea, Vol. 2. Interscience, New York, pp. 26–77.

Renfrew, I.A., Pickart, R.S., Våge, K., Moore, G.W.K., Bracegirdle, T.J., Elvidge, A.D., Jeansson, E., Lachlan-Cope, T., McRaven, L., Papritz, L., Reuder, J., Sodemann, H., Terpstra, A., Waterman, S., Valdimarsson, H., Weiss, A., Almansi, M., Bahr, F., Brakstad, A., Barrell, C., Brooke, J.K., Brooks, B.J., Brooks, I.M., Brooks, M.E., Bruvik, E.M., Duscha, C., Fer, I., Golid, H.M., Hallerstig, M., Hessevik, I., Huang, J., Houghton, L., Jónsson, S., Jonassen, M., Jackson, K., Kvalsund, K., Kolstad, E.W., Konstali, K., Kristiansen, J., Ladkin, R., Lin, P., Macrander, A., Mitchell, A., Olafsson, H., Pacini, A., Payne, C., Palmason, B., Pérez-Hernándes, M.D., Peterson, A.K., Petersen, G.N., Pisareva, M.N., Pope, J.O., Seidl, A., Semper, S., Sergeev, D., Skjelsvik, S., Søiland, H., Smith, D., Spall, M.A., Spengler, T., Touzeau, A., Tupper, G., Weng, Y., Williams, K.D., Yang, X., Zhou, S., 2019. The Iceland Greenland Seas project. Bull. Am. Meteorol. Soc. 100 (9), 1795–1817. http://dx.doi.org/10.1175/BAMS-D-18-0217.1.

Ronski, S., Budéus, G., 2005. Time series of winter convection in the Greenland Sea. J. Geophys. Res. 110 (C4), http://dx.doi.org/10.1029/2004jc002318.

Rossby, T., Flagg, C., Chafik, L., Harden, B., Søiland, H., 2018. A direct estimate of volume, heat, and freshwater exchange across the Greenland–Iceland–Faroe–Scotland Ridge. J. Geophys. Res.: Oceans 123 (10), 7139–7153. http://dx.doi.org/10.1029/2018JC014250.

Rudels, B., Björk, G., Nilsson, J., Winsor, P., Lake, I., Nohr, C., 2005. The interaction between waters from the Arctic Ocean and the Nordic Seas north of Fram Strait and along the East Greenland Current: results from the Arctic Ocean-02 Oden expedition. J. Mar. Syst. 55 (1–2), 1–30. http://dx.doi.org/10.1016/j.jmarsys.2004.06.008.

Rudels, B., Fahrbach, E., Meincke, J., Budéus, G., Eriksson, P., 2002. The East Greenland Current and its contribution to the Denmark strait overflow. ICES J. Mar. Sci. 59 (6), 1133–1154. http://dx.doi.org/10.1006/jmsc.2002.1284.

Rudels, B., Friedrich, H.J., Quadfasel, D., 1999. The Arctic circumpolar boundary current. Deep-Sea Res. II 46 (6–7), 1023–1062. http://dx.doi.org/10.1016/S0967-0645(99)00015-6.

Saberi, A., Haine, T.W.N., Gelderloos, R., Femke de Jong, M., Furey, H., Bower, A., 2020. Lagrangian perspective on the origins of Denmark Strait Overflow. J. Phys. Oceanogr. 50 (8), 2393–2414. http://dx.doi.org/10.1175/JPO-D-19-0210.1.

Schlitzer, R., 2007. Assimilation of radiocarbon and chlorofluorocarbon data to constrain deep and bottom water transports in the world ocean. J. Phys. Oceanogr. 37 (2), 259–276. http://dx.doi.org/10.1175/JPO3011.1.

Schlosser, P., Bönisch, G., Rhein, M., Bayer, R., 1991. Reduction of deepwater formation in the Greenland Sea during the 1980s: Evidence from tracer data. Science 251 (4997), 1054–1056. http://dx.doi.org/10.1126/science.251.4997.1054.

Semper, S., Pickart, R.S., Våge, K., Larsen, K.M.H., Hansen, B., Hátún, H., 2020. The Iceland-Faroe Slope Jet: a conduit for dense water toward the Faroe Bank Channel overflow. Nature Commun. 11 (5390), http://dx.doi.org/10.1038/s41467-020-19049-5.

Semper, S., Våge, K., Pickart, R.S., Jónsson, S., Valdimarsson, H., 2022. Evolution and transformation of the North Icelandic Irminger Current along the north Iceland shelf. J. Geophys. Res.: Oceans 127 (3), e2021JC017700. http://dx.doi.org/10.1029/2021JC017700.

Semper, S., Våge, K., Pickart, R.S., Valdimarsson, H., Torres, D.J., Jónsson, S., 2019. The emergence of the North Icelandic Jet and its evolution from northeast Iceland to Denmark Strait. J. Phys. Oceanogr. (2019), http://dx.doi.org/10.1175/JPO-D-19-0088.1.

Serra, N., Käse, R.H., Kähl, A., Stammer, D., Quadfasel, D., 2010. On the low-frequency phase relation between the Denmark Strait and the Faroe-Bank Channel overflows. Tellus A 62 (4), 530–550. http://dx.doi.org/10.1111/j.1600-0870.2009.00445.x.

Shao, Q., Zhao, J., Drinkwater, K.F., Wang, X., Cao, Y., 2019. Internal overflow in the Nordic Seas and the cold reservoir in the northern Norwegian Basin. Deep-Sea Res. I 148, 67–79. http://dx.doi.org/10.1016/j.dsr.2019.04.012.

Skagseth, Ø., Mork, K.A., 2012. Heat content in the Norwegian Sea, 1995 - 2010. ICES J. Mar. Sci. 69 (5), 826–832. http://dx.doi.org/10.1093/icesjms/fss026.

Smedsrud, L.H., Muilwijk, M., Brakstad, A., Madonna, E., Lauvset, S.K., Spensberger, C., Born, A., Eldevik, T., Drange, H., Jeansson, E., Li, C., Olsen, A., Skagseth, Ø., Slater, D.A., Straneo, F., Våge, K., Årthun, M., 2022. Nordic Seas heat loss, Atlantic inflow, and Arctic sea ice cover over the last century. Rev. Geophys. 60 (1), e2020RG000725. http://dx.doi.org/10.1029/2020RG000725.

Somavilla, R., 2019. Draining and upwelling of Greenland Sea deep waters. J. Geophys. Res.: Oceans 124, 2842–2860. http://dx.doi.org/10.1029/2018JC014249.

Somavilla, R., Schauer, U., Budeus, G., 2013. Increasing amount of Arctic Ocean deep waters in the Greenland Sea. Geophys. Res. Lett. 40 (16), 4361–4366. http://dx.doi.org/10.1002/grl.50775.

Strass, V.H., Fahrbach, E., Schauer, U., Sellmann, L., 1993. Formation of Denmark Strait overflow water by mixing in the East Greenland Current. J. Geophys. Res. 98 (C4), 6907–6919. http://dx.doi.org/10.1029/92JC02732.

Swift, J.H., Aagaard, K., 1981. Seasonal transitions and water mass formation in the Iceland and Greenland seas. Deep-Sea Res. A 28 (10), 1107–1129. http://dx.doi.org/10.1016/0198-0149(81)90050-9.

Swift, J.H., Aagaard, K., Malmberg, S.A., 1980. The contribution of the Denmark Strait overflow to the deep North Atlantic. Deep-Sea Res. A 27 (1), 29–42. http://dx.doi.org/10.1016/0198-0149(80)90070-9.

Swift, J.H., Koltermann, K.P., 1988. The origin of Norwegian Sea deep water. J. Geophys. Res.: Oceans 93 (C4), 3563–3569. http://dx.doi.org/10.1029/JC093iC04p03563.

Tanhua, T., Olsson, K.A., Jeansson, E., 2005. Formation of Denmark Strait overflow water and its hydro-chemical composition. J. Mar. Syst. 57 (3–4), 264–288. http://dx.doi.org/10.1016/j.jmarsys.2005.05.003.

Tsubouchi, T., Våge, K., Hansen, B., Larsen, K.M.H., Østerhus, S., Johnson, C., Jónsson, S., Valdimarsson, H., 2021. Increased ocean heat transport into the Nordic Seas and Arctic Ocean over the period 1993–2016. Nature Clim. Change 11, 21–26. http://dx.doi.org/10.1038/s41558-020-00941-3.

Turrell, W.R., Slesser, G., Adams, R.D., Payne, R., Gillibrand, P.A., 1999. Decadal variability in the composition of Faroe Shetland Channel bottom water. Deep-Sea Res. I 46 (1), 1–25. http://dx.doi.org/10.1016/S0967-0637(98)00067-3.

Våge, K., Moore, G.W.K., Jónsson, S., Valdimarsson, H., 2015. Water mass transformation in the Iceland Sea. Deep-Sea Res. I 101, 98–109. http://dx.doi.org/10.1016/j.dsr.2015.04.001.

Våge, K., Papritz, L., Håvik, L., Spall, M.A., Moore, G.W.K., 2018. Ocean convection linked to the recent ice edge retreat along east Greenland. Nature Commun. 9, 1287. http://dx.doi.org/10.1038/s41467-018-03468-6.

Våge, K., Pickart, R.S., Spall, M.A., Moore, G.W.K., Valdimarsson, H., Torres, D.J., Erofeeva, S.Y., Nilsen, J.E.Ø., 2013. Revised circulation scheme north of the Denmark Strait. Deep-Sea Res. I 79, 20–39. http://dx.doi.org/10.1016/j.dsr.2013.05.007.

Våge, K., Pickart, R.S., Spall, M.A., Valdimarsson, H., Jónsson, S., Torres, D.J., Østerhus, S., Eldevik, T., 2011. Significant role of the North Icelandic Jet in the formation of Denmark Strait overflow water. Nat. Geosci. 4 (10), 723–727. http://dx.doi.org/10.1038/ngeo1234.

Våge, K., Semper, S., Valdimarsson, H., Jónsson, S., Pickart, R.S., Moore, G.W.K., 2022. Water mass transformation in the Iceland Sea: Contrasting two winters separated by four decades. Deep-Sea Res. I 186, 103824. http://dx.doi.org/10.1016/j.dsr.2022.103824.

Voet, G., Quadfasel, D., Mork, K.A., Søiland, H., 2010. The mid - depth circulation of the Nordic Seas derived from profiling float observations. Tellus A 62 (4), 516–529. http://dx.doi.org/10.1111/j.1600-0870.2009.00444.x.

Walsh, J.E., Chapman, W.L., Fetterer, F., 2015. Gridded Monthly Sea Ice Extent and Concentration, 1850 Onwards, Version 1. National Snow and Ice Data Center, Boulder, Colorado USA, http://dx.doi.org/10.7265/N5833PZ5.

Walsh, J.E., Fetterer, F., Stewart, J.S., Chapman, W.L., 2017. A database for depicting Arctic sea ice variations back to 1850. Geogr. Rev. 107 (1), 89–107. http://dx.doi.org/10.1111/j.1931-0846.2016.12195.x.

Wang, X., Zhao, J., Hattermann, T., Lin, L., Chen, P., 2021. Transports and accumulations of Greenland Sea intermediate waters in the Norwegian Sea. J. Geophys. Res.: Oceans 126 (4), e2020JC016582. http://dx.doi.org/10.1029/2020JC016582.